Current Biology

Article

Calponin isoforms define the cell-type-specific organization and dynamics of actomyosin bundles

Graphical abstract

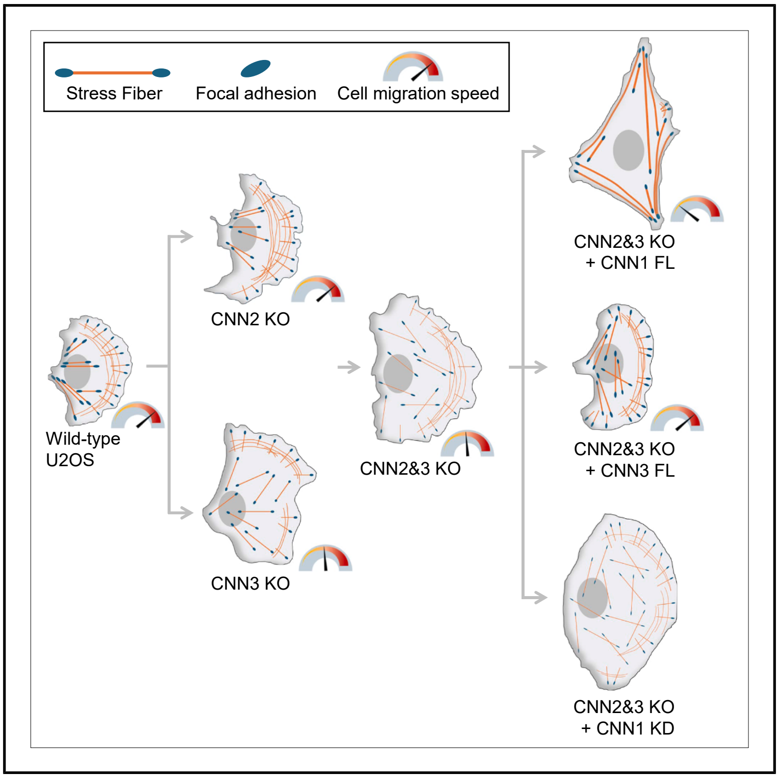

Highlights

- Calponins control stress fiber architecture, cell migration, and morphogenesis
- Calponins regulate the distribution and dynamics of α-actinin along stress fibers
- Calponins are not negative regulators of myosin II activity
- Calponins control stress fiber organization in an isoform-specific manner

Authors

Shrikant B. Kokate, Afsana T. Oshin, Xiang Le Chua, ..., Teemu Tomberg, Johanna Ivaska, Pekka Lappalainen

Correspondence

shrikant.kokate@helsinki.fi (S.B.K.),
pekka.lappalainen@helsinki.fi (P.L.)

In brief

Kokate et al. show that calponins regulate the architecture of actomyosin bundles. Their loss results in abnormal distribution of α-actinin, reduced thickness of actomyosin bundles, and impaired cell migration. Non-muscle and smooth-muscle calponin isoforms display different dynamics and hence have different effects on the organization and dynamics of actomyosin bundles.

Kokate et al., 2025, Current Biology *35*, 1–14
December 15, 2025
https://doi.org/10.1016/j.cub.2025.10.081

CellPress

Please cite this article in press as: Kokate et al., Calponin isoforms define the cell-type-specific organization and dynamics of actomyosin bundles, Current Biology (2025), https://doi.org/10.1016/j.cub.2025.10.081

Current Biology

CellPress
OPEN ACCESS

Article

Calponin isoforms define the cell-type-specific organization and dynamics of actomyosin bundles

Shrikant B. Kokate,[1,2,9,*] **Afsana T. Oshin,**[1,2] **Xiang Le Chua,**[1,2] **Megan Chastney,**[3] **Parijat Biswas,**[1,2] **Konstantin Kogan,**[1,2] **Teemu Tomberg,**[4,5] **Johanna Ivaska,**[3,6,7,8] **and Pekka Lappalainen**[1,2,9,10,*]
[1]HiLIFE Institute of Biotechnology, University of Helsinki, 00014 Helsinki, Finland
[2]Faculty of Biological and Environmental Sciences, University of Helsinki, 00014 Helsinki, Finland
[3]Turku Bioscience Centre, University of Turku and Åbo Akademi University, 20520 Turku, Finland
[4]Division of Pharmaceutical Chemistry and Technology, Faculty of Pharmacy, University of Helsinki, 00014 Helsinki, Finland
[5]Department of Chemistry, Faculty of Science, University of Helsinki, 00014 Helsinki, Finland
[6]Department of Life Technologies, University of Turku, 20014 Turku, Finland
[7]InFLAMES Research Flagship Center, University of Turku, 20014 Turku, Finland
[8]Foundation for the Finnish Cancer Institute, 00290 Helsinki, Finland
[9]Present address: Molecular and Integrative Biosciences Research Programme, Faculty of Biological and Environmental Sciences & HiLIFE Institute of Biotechnology, P.O. Box 56, Viikinkaari 5, University of Helsinki, 00014 Helsinki, Finland
[10]Lead contact
*Correspondence: shrikant.kokate@helsinki.fi (S.B.K.), pekka.lappalainen@helsinki.fi (P.L.)
https://doi.org/10.1016/j.cub.2025.10.081

SUMMARY

Contractile actomyosin bundles, stress fibers, are important for cell migration, adhesion, morphogenesis, and mechanosensing. Calponin (CNN) family proteins are abundant stress fiber components, but their cellular functions and isoform-specific roles remain poorly understood. By depleting the three CNN isoforms (calponin-1 [CNN1], calponin-2 [CNN2], and calponin-3 [CNN3]) individually and collectively from U2OS cells, we show that CNNs are not negative regulators of myosin II, as previously suggested. Instead, we reveal that CNNs are critical regulators of stress fiber organization that control the distribution of actin filament cross-linker, α-actinin, along actomyosin bundles. Consequently, loss of CNNs dramatically reduced stress fiber thickness, increased their fragility, and impaired cell migration. Notably, we also identify isoform-specific roles for CNNs. The non-muscle CNN isoform CNN3 displays rapid turnover in stress fibers, enabling their dynamic remodeling, whereas the smooth-muscle isoform CNN1 exhibits stable association with stress fibers, supporting the formation of "smooth-muscle-like" thick and static actomyosin bundles. Our findings highlight CNNs as key regulators of stress fiber architecture, cell migration, and morphogenesis and provide new insights into the functional diversity of smooth-muscle and non-muscle CNN isoforms.

INTRODUCTION

Stress fibers are contractile actomyosin bundles, which have important roles in morphogenesis, adhesion, and migration of non-muscle cells. Stress fibers are also among the most prominent mechanosensitive structures in many cell types because they scale with rigidity: stress fibers are typically very thin and disorganized in cells grown on a soft extracellular matrix but become thicker and reinforced when cells experience a stiff environment or external forces.[1–3]

Consequently, disruption of stress fibers results in defective cellular mechanotransduction.[4] At the molecular level, stress fibers are composed of regular arrays of α-actinin cross-linked actin filaments and bipolar non-muscle myosin II (NM2) filaments, and are hence considered to resemble the striated muscle myofibrils. This is also supported by studies demonstrating that stress fibers of non-muscle cells and myofibrils of striated muscles are assembled through a similar mechanism, which involves the generation of mature actomyosin bundles from more dynamic and less organized precursors called transverse arcs.[5–9] However, stress fibers lack many key structural components of muscle myofibrils and do not contain the troponin complex, which is responsible for Ca^{2+}-regulated contractility of striated muscles.[1] Therefore, the mechanisms by which myosin II activity is controlled in stress fibers have remained elusive. On the other hand, stress fibers contain a large array of other actin- and NM2-associated proteins, which regulate the assembly and stability of actin filaments[10–16] or proper folding and distribution of NM2-filament stacks along the stress fibers.[17–19] Additionally, stress fibers harbor many proteins, whose functions are still poorly understood.

Among the conserved stress fiber components whose functions have remained enigmatic are the calponin family proteins. Although identified nearly 40 years ago,[20] the specific roles of calponins in controlling the organization, dynamics, and contractility of actomyosin bundles have remained controversial.[21] At the molecular level, calponins have been suggested to function as stabilizers of actin filaments, regulators of myosin II, scaffolding proteins for ERK signaling, or regulators of another stress fiber component, caldesmon.[21] However, these proposed

Please cite this article in press as: Kokate et al., Calponin isoforms define the cell-type-specific organization and dynamics of actomyosin bundles, Current Biology (2025), https://doi.org/10.1016/j.cub.2025.10.081

functions of calponins are largely based on biochemical studies, and their relevance in the cellular context has remained unclear. For example, according to the "popular view," calponins function as negative regulators of the ATPase activity of myosin II by binding to actin filaments and preventing the motor domain of myosin II from interacting with actin.[22] However, whether calponins indeed regulate myosin II activity in non-muscle and smooth-muscle cells, like the troponin complex in striated muscles, has not been experimentally demonstrated.

Uncovering the cellular function of calponins is further complicated by the presence of three isoforms in vertebrates that may display redundant functions with each other. They are composed of an N-terminal calponin homology (CH) domain and an unstructured, actin-binding C-terminal half that contains three calponin-like (CLIK) repeats.[23] Also invertebrates have calponin homologues, but their domain organization is somewhat different from vertebrate calponins.[24] The three vertebrate calponins are highly homologous to each other, and display major differences only at their very C-terminal region following the CLIK repeats.[21] The shortest isoform is calponin-1 (CNN1), which is mainly expressed in smooth-muscle cells. Knockout studies demonstrated that CNN1 is not an essential component of smooth-muscle contractility.[25] However, CNN1 knockout mice showed abnormally fast contractile velocity of smooth muscles[26] and reduced smooth-muscle cell sensitivity to agonist stimulation,[27,28] indicating that CNN1 either directly or indirectly contributes to proper contractility of smooth muscles. The two other isoforms, calponin-2 (CNN2) and calponin-3 (CNN3), are predominantly expressed in non-muscle tissues and differ from CNN1 by having C-terminal extensions composed of negatively charged amino acids.[21] CNN2 knockout mice are viable but exhibit defects in motility and phagocytosis in macrophages.[29,30] Deletion of the ubiquitous non-muscle isoform, CNN3, results in embryonic lethality.[31] In cultured cells, CNN2 and CNN3 localize to stress fibers, but their depletions typically result in relatively modest effects in the organization of stress fibers, suggesting possible functional redundancy between these calponin isoforms.[32–35] One of the prevailing views in the field is that calponins regulate actomyosin bundles through inhibition of myosin II. However, owing to conflicting reports of CNN2 or CNN3 depletions resulting in either increased or decreased traction forces, their mechanism of action in cells remains poorly understood.[33–35] Moreover, CNN3 localization overlaps with α-actinin, not with myosin II, in stress fibers, suggesting an indirect role in regulating stress fiber contractility and accompanied traction forces.[33] Thus, the actual mechanism by which calponins regulate actomyosin bundles of smooth muscles and stress fibers of non-muscle cells, as well as the possible isoform-specific roles of different calponins, have remained elusive.

RESULTS

Non-muscle calponin isoforms are functionally redundant with each other in cell migration, invasion, and actin organization

CNN1 is mainly expressed in smooth muscles, whereas CNN2 and CNN3 are present in a broad range of tissues and cell types.[36–43] Both isoforms localize to actin stress fiber networks,[9,33,39] but whether CNN2 and CNN3 co-localize with each other in different types of stress fibers, and display specific or redundant roles in cells, has not been reported. By using a CNN2-specific antibody combined with expressing mScarlet-tagged CNN3 in U2OS cells, we revealed that CNN2 and CNN3 co-localize with each other in different categories of stress fibers: transverse arcs, dorsal stress fibers, and ventral stress fibers (Figure 1A). We next utilized the CRISPR-Cas9 approach to generate CNN2 and CNN2&3 knockout U2OS cells using three different guide RNAs targeting the first exon of CNN2. For the CNN2&3 double knockouts, we used a CNN3 knockout cell line from a previous study as a starting point.[33] The successful knockouts were confirmed at the protein level by western blotting and at the genomic level by Sanger and next-generation sequencing (Figures S1A–S1K). High-throughput image analysis of phalloidin and DAPI-stained cells revealed that depletion of CNN2 did not result in drastic effects on cell shape or random migration of individual cells, whereas the CNN3 knockout and CNN2&3 double-knockout cells displayed slower migration velocity and were slightly more elongated as compared with the wild-type U2OS cells (Figures 1B–1D). A wound healing assay demonstrated that, whereas the CNN2 knockout cells displayed only a very modest defect in collective migration, the CNN3 knockout cells exhibited more pronounced problems in collective cell migration, and these were more prominent in the CNN2&3 double-knockout cells (Figures 1E and 1F). Thus, CNN3 appears to be more important for cell migration in U2OS cells as compared with CNN2, and this may be due to differences in the expression levels of these two proteins. The functional redundancy between CNN2 and CNN3 was most clearly demonstrated by a transwell Matrigel cell invasion assay, where both CNN2 and CNN3 knockout cells displayed only relatively modest defects, whereas the CNN2&3 double-knockout cells were nearly completely defective in cell invasion (Figures 1G and 1H).

We next analyzed the organization of the actin cytoskeleton in the wild-type and the three knockout cell lines. Visualizing α-actinin, NM2, focal adhesions, and actin filaments suggested that stress fiber networks appeared relatively normal in the CNN2 knockout cells and were slightly less organized in the CNN3 knockout cells. However, the CNN2&3 double-knockout cells displayed more pronounced defects, as their stress fibers appeared thinner and less organized compared with the wild-type cells and to the cells lacking either CNN2 or CNN3 (Figures S2A–S2F). Please note that, to be able to compare the organization of actin networks in wild-type and knockout cells from the same fields of view, these experiments were carried out by mixing the CNN2, CNN3, and CNN2&3 knockout cells with wild-type cells stably expressing EGFP-CAAX. The lack of clear stress fiber phenotype was confirmed from several CNN2 knockout clones generated with different guide RNAs, and the characterization of different CNN2&3 double-knockout clones will be discussed in the following chapters.

Western blot analysis revealed that both wild-type cells and the CNN2&3 double-knockout clone selected for these initial studies (clone "G3 CL1"; Figures S1K and S1L) also expressed low levels of smooth-muscle calponin isoform CNN1. To study how the loss of all calponin isoforms affects stress fiber networks, we generated calponin-null cells by small interfering RNA (siRNA)-mediated silencing of CNN1 from the CNN2&3

Please cite this article in press as: Kokate et al., Calponin isoforms define the cell-type-specific organization and dynamics of actomyosin bundles, Current Biology (2025), https://doi.org/10.1016/j.cub.2025.10.081

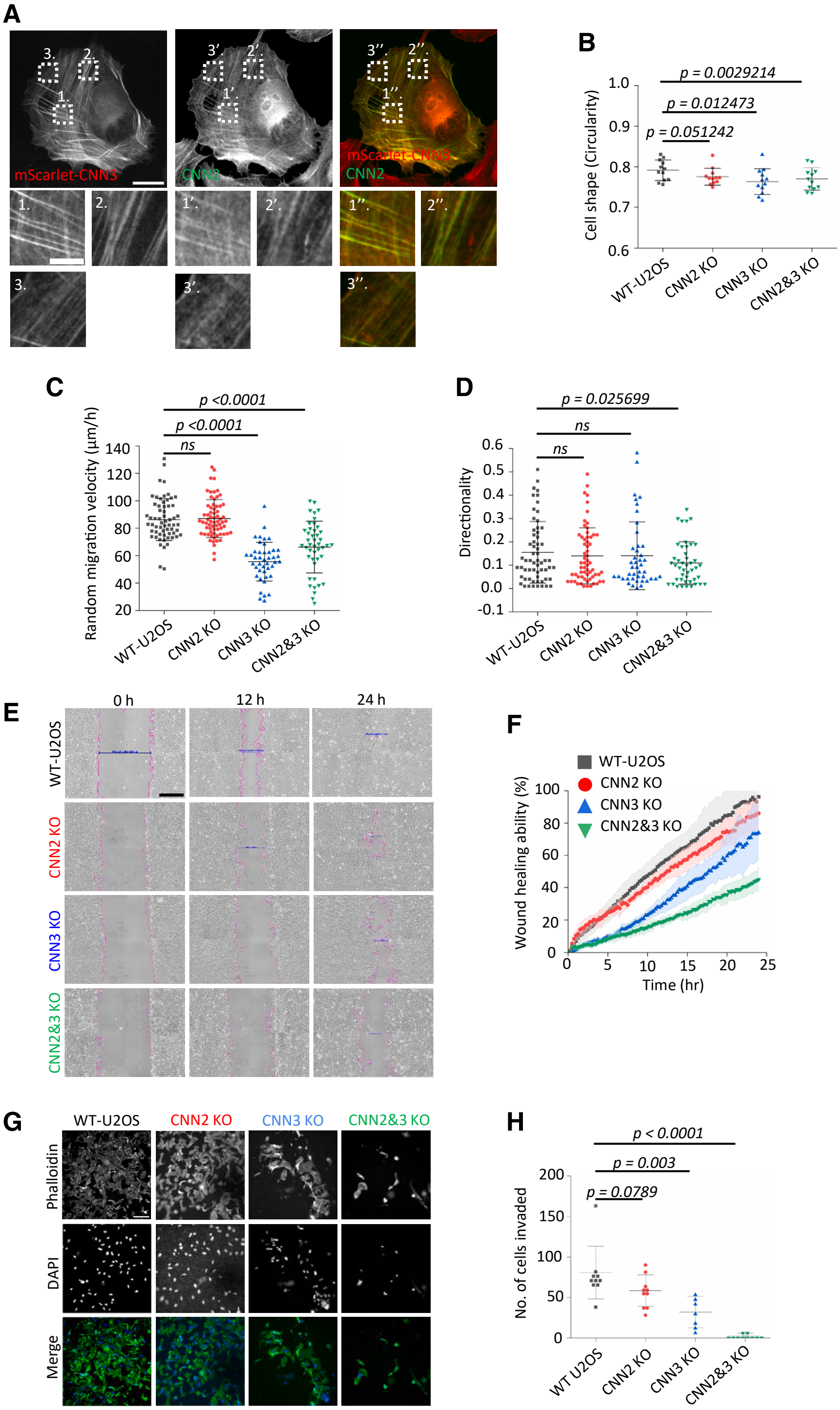

Figure 1. Calponins have redundant roles in migration, invasion, and morphogenesis of U2OS cells

(A) Representative fluorescence microscopy images showing the co-localization of CNN2 and CNN3 in different types of stress fibers of U2OS cells transfected with mScarlet-CNN3 plasmid and stained with CNN2-specific antibody. White dashed boxes and their zoomed-in images below indicate the co-localization of CNN2 and CNN3 in dorsal stress fibers (SFs) (1 and 1′), ventral SFs (2 and 2′), and transverse arcs (3 and 3′). Scale bars, 20 and 5 μm, respectively.

(B) Cell shape analyses of wild-type, CNN2 knockout (KO), CNN3 KO, and CNN2&3 double-KO U2OS cells. Data represent mean ± SD of n = 7,938 (wild-type), 14,321 (CNN2 KO), 12,207 (CNN3 KO), and 14,775 (CNN2&3 KO) cells. Each data point represents the mean value of a single well from a 96-well plate.

(C and D) (C) Graphical representation of random migration velocity and (D) directionality of wild-type (n = 57), CNN2 KO (n = 63), CNN3 KO (n = 39), and CNN2&3 KO (n = 40) cells. Data represent mean ± SD from three experiments.

(E) Representative examples of a wound healing assay demonstrating the scratch area covered by wild-type and KO cells at 0, 12, and 24 h after wound creation. Scale bars, 200 μm.

(F) Graphical analysis of the percentage (%) of wound area covered by wild-type and KO cells. Data are presented as mean ± SD from three experiments.

(G) Representative Matrigel invasion assay images of wild-type and KO cells demonstrating the amount of cells invaded through the transwell chamber. Scale bar, 100 μm.

(H) Analysis of the number of wild-type and KO cells invaded through transwell Matrigel insert. Data represent mean ± SD, and each data point represents the number of invaded cells measured per field of view obtained from three different experiments.

See also Figure S1.

double-knockout cells (Figures 2A and 2B). Cells were stained with fluorescent phalloidin to visualize actin filaments and vinculin-specific antibody to visualize focal adhesions. Interestingly, silencing CNN1 from the CNN2&3 double-knockout cells resulted in severely disorganized stress fiber networks (Figures 2C and 2D). Blind analysis of phalloidin-stained images of cells having either “thin,” “moderate,” or “thick” stress fibers revealed that simultaneous depletion of CNN2 and CNN3 led to more pronounced thinning of stress fibers as compared with individual CNN2 or CNN3 knockouts, and that this phenotype was further worsened by silencing of CNN1. Similar results were also obtained from an analysis performed by the Ridge detection plugin from Fiji ImageJ, although this analysis did not reveal a difference between the CNN2&3 double-knockout cells and the CNN1-silenced CNN2&3 double-knockout cells (Figures S2G, S2H, and S2K). Moreover, blind analysis provided evidence that the alignment of stress fibers was also severely defective in the CNN1-silenced CNN2&3 double-knockout cells (Figures 2E, 2F, S2L, and S2M). On the other hand, loss of calponins did not result in drastic effects on focal adhesion number, although adhesions were smaller and less elongated in all calponin-depleted clones analyzed here, and these phenotypes appeared

Please cite this article in press as: Kokate et al., Calponin isoforms define the cell-type-specific organization and dynamics of actomyosin bundles, Current Biology (2025), https://doi.org/10.1016/j.cub.2025.10.081

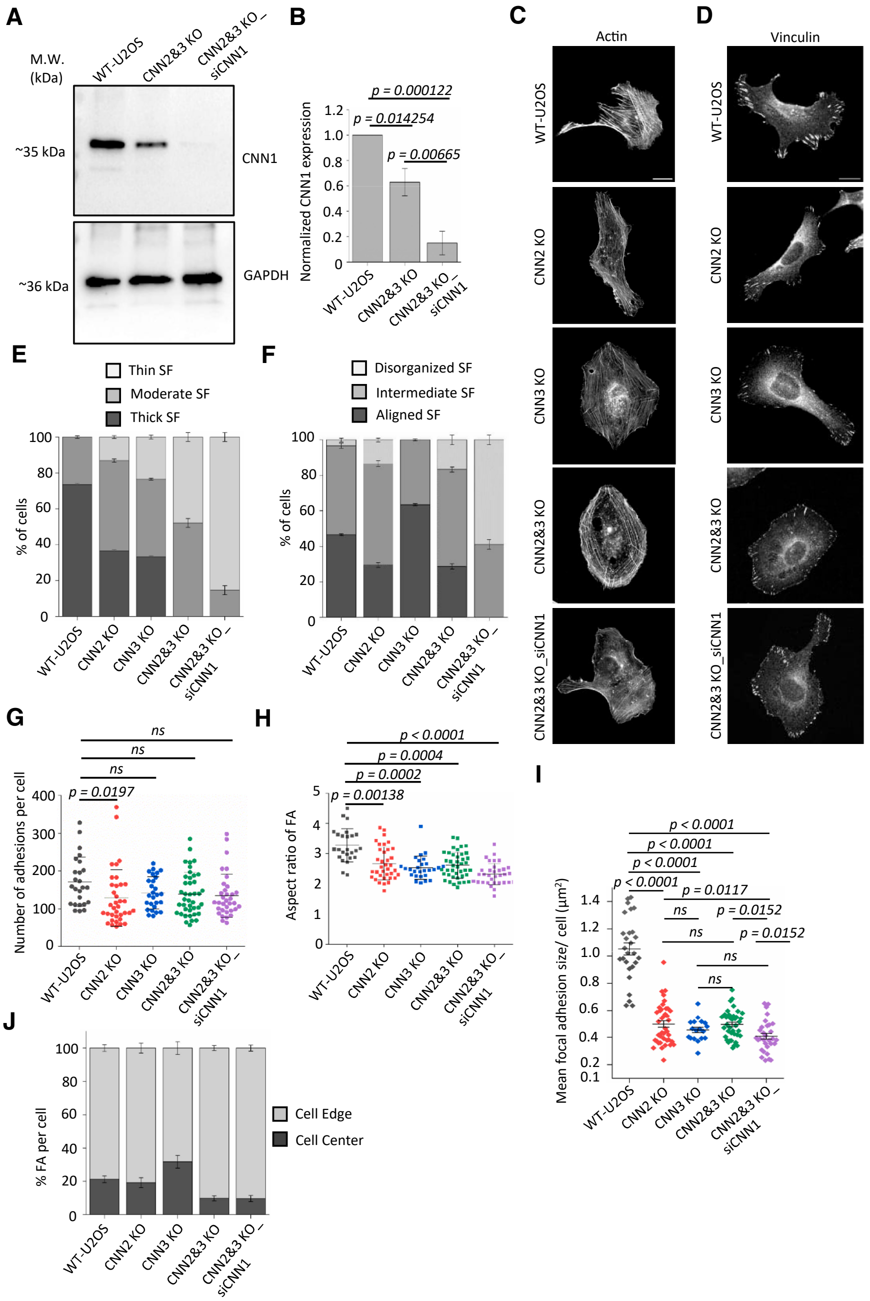

Figure 2. Calponin-null cells have thin and disorganized SFs

(A) Representative western blot image showing the protein levels of CNN1 in wild-type and CNN2&3 KO, as well as in the CNN2&3 KO cells transfected with CNN1-specific siRNA. GAPDH was used as a loading control.

(B) Bar graphs of CNN1 protein levels. Data represent mean ± SEM from four experiments.

(C and D) Representative wide-field microscopy images of wild-type, CNN2 KO, CNN3 KO, CNN2&3 KO, and CNN2&3 KO_siCNN1 cells stained with fluorescent phalloidin and anti-vinculin antibody to highlight the organization of actin SFs and focal adhesions, respectively. Scale bars, 20 μm.

(E) Blind analysis of the percentage of thin, intermediate, and thick SFs in wild-type ($n = 30$), CNN2 KO ($n = 30$), CNN3 KO ($n = 30$), CNN2&3 KO ($n = 31$), and CNN2&3 KO_siCNN1 ($n = 30$) cells from three experimental repeats. The error bars represent mean ± SEM.

(F) Blind analysis of the percentage of cells having disorganized, intermediate, and aligned SFs. Wild-type ($n = 30$), CNN2 KO ($n = 30$), CNN3 KO ($n = 30$), CNN2&3 KO ($n = 31$), and CNN2&3 KO_siCNN1 ($n = 30$) cells from three experimental repeats. The error bars represent mean ± SEM.

(G and H) Quantification of the focal adhesion numbers and aspect ratios from wild-type ($n = 25$), CNN2 KO ($n = 36$), CNN3 KO ($n = 27$), CNN2&3 KO ($n = 41$), and CNN2&3 KO_siCNN1 ($n = 34$) cells from three experimental repeats. Each data point in the graph represents the mean value from a single cell. Groups were compared with Kruskal-Wallis ANOVA followed by Dunn's multiple comparison test. The p values were adjusted for multiple comparisons. The error bars represent mean ± SEM.

(I) Size distributions of focal adhesions in wild-type ($n = 25$), CNN2 KO ($n = 36$), CNN3 KO ($n = 27$), CNN2&3 KO ($n = 41$), and CNN2&3 KO_siCNN1 ($n = 33$) cells analyzed from three experimental repeats. The error bars represent mean ± SEM.

(J) Distributions of focal adhesions at the cell edge (within 5 μm from the leading edge) vs. cell center in wild-type ($n = 21$), CNN2 KO ($n = 36$), CNN3 KO ($n = 27$), CNN2&3 KO ($n = 35$), and CNN2&3 KO_siCNN1 ($n = 27$) cells from three repeats. The error bars represent mean ± SEM.

See also Figure S2.

most pronounced in the CNN1-silenced CNN2&3 double-knockout cells (Figures 2G–2I). Moreover, adhesions in the CNN2&3 double-knockout and CNN1-silenced CNN2&3 double-knockout cells were more often concentrated at cell edges as compared with wild-type and individual knockout cells (Figures 2J, S2I, and S2J).

Previous biochemical studies suggested that calponins can also stabilize actin filaments.[44],[45] Moreover, CNN3 knockout cells were reported to exhibit increased stress fiber breakage events.[33] Consistent with this earlier study, the abnormally thin stress fibers in the CNN2&3 double-knockout cells (both in the presence and absence of CNN1) were more fragile as compared with the stress fibers of wild-type cells. This is because quantitative analysis of 30 min time-lapse videos of cells expressing EGFP-Lifeact revealed an ∼10-fold increase in stress fiber breakage events in CNN2&3 double-knockout and CNN1-silenced double-knockout cells as compared with wild-type cells, and this phenotype could be partially rescued by expressing either CNN1 or CNN3 in the double-knockout cells (Figure 3). However, our fluorescence recovery after photobleaching (FRAP) experiments revealed that the dynamics of actin in stress fibers were not significantly altered in the absence of CNN2 and CNN3 (Figures S3A–S3D). Thus, calponins do not appear to stabilize actin filaments, but in the absence of calponins, the architecture of stress fibers is compromised in a way that results in their aberrant breakage or regional disassembly.

Please cite this article in press as: Kokate et al., Calponin isoforms define the cell-type-specific organization and dynamics of actomyosin bundles, Current Biology (2025), https://doi.org/10.1016/j.cub.2025.10.081

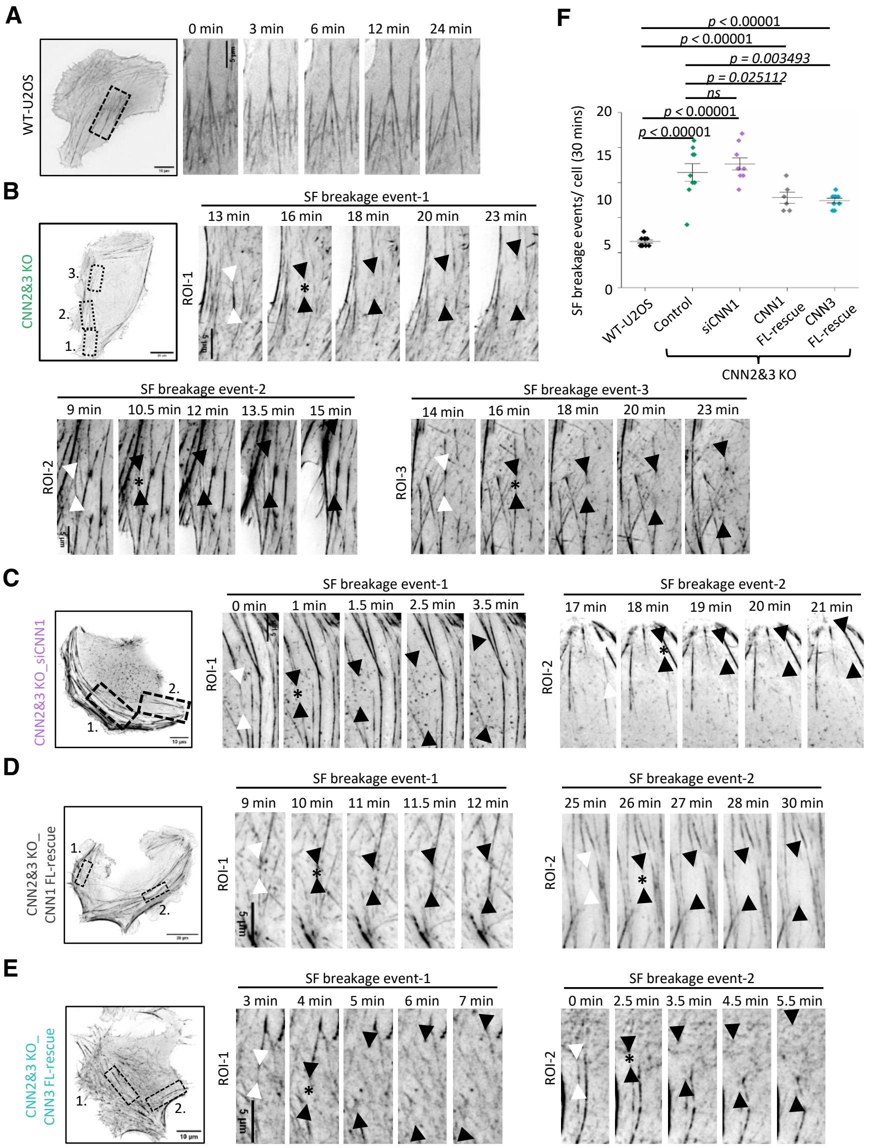

Figure 3. Loss of calponins increases SF fragility

(A–E) Representative time-lapse microscopy images of (A) wild-type, (B) CNN2&3 KO, (C) CNN2&3 KO_siCNN1, and CNN2&3 KO cells rescued with plasmids expressing full-length (D) EGFP-CNN1 and (E) EGFP-CNN3. Examples of SF breakage events are indicated in the time-lapse images (from the boxed regions of the whole-cell images) with an asterisk (*), and the black arrowheads highlight the movement of the ends of severed SFs. The white arrowheads in the first time-lapse images highlight the SFs becoming severed. Scale bars, 10 and 5 μm, respectively.

(F) Quantification of the total number of SF breakage events in wild-type ($n = 10$), CNN2&3 KO ($n = 9$), and CNN2&3 KO_siCNN1 ($n = 9$) cells, as well as in CNN2&3 KO cells rescued with EGFP-CNN1 ($n = 6$) and EGFP-CNN3 ($n = 9$) plasmids from 30 imaging periods. Data represent mean ± SEM.

See also Figure S3.

Together, these experiments demonstrate that the non-muscle calponin isoforms, CNN2 and CNN3, display overlapping functions in regulating stress fiber architecture, cell migration, and cell invasion. Depletion of the remaining CNN1 further enhances the disturbed cytoskeleton phenotype. Hence, the loss of all three calponin isoforms leads to a nearly complete loss of thick stress fibers and severely disorganized architecture of the remaining stress fiber network.

Calponins are not negative regulators of actomyosin contractility in non-muscle cells

Previous studies suggested that calponins function as negative regulators of actomyosin contractility either by directly inhibiting actin-myosin interaction or by functioning as scaffolding proteins that control the association of another actomyosin bundle component, caldesmon, with actin filaments.[26,36,46–49] However, because these models are largely based on biochemical studies, and because the effects of simultaneous depletion of all calponin isoforms on actomyosin contractility have not been reported, we decided to re-examine the possible role of calponins in actomyosin contractility. The assembly of myosin IIa and IIb into bipolar arrays was not affected in the CNN2&3 double-knockout cells (Figures S4A–S4J). The dynamics of myosin IIa in stress fibers (as measured by FRAP) was not affected upon depletion of CNN2 and CNN3, whereas myosin IIb displayed slightly more rapid dynamics in the stress fibers of CNN2&3 double-knockout cells as compared with wild-type cells (Figures S4K–S4P). Interestingly, traction force microscopy (TFM) revealed that CNN2&3 double-knockout cells, as well as the CNN1-silenced double-knockout cells lacking all three calponin isoforms, did not exhibit increased traction forces as would be expected if calponins would function as negative regulators of actomyosin contractility. Instead, the traction forces were diminished in these knockout/knockdown cells (Figures 4A and 4B). Because decreased traction forces could, in principle, result from the breakage of stress fibers, we examined the role of calponins in actomyosin contractility also by another approach. First, we measured the rate of retrograde flow of transverse arcs. These contractile actomyosin bundles assemble at the leading edge of the cell and undergo myosin II-powered retrograde flow toward the cell center.[6,50] Consistent with the TFM analysis described above, kymograph analysis of time-lapse images from wild-type and CNN2&3 double-knockout cells expressing GFP-Lifeact revealed that the velocity of transverse arc retrograde flow was reduced in the double knockouts as compared with the wild-type cells (Figures 4C–4E). Second, we performed laser-ablation experiments on U2OS cells cultured on crossbow-shaped

Please cite this article in press as: Kokate et al., Calponin isoforms define the cell-type-specific organization and dynamics of actomyosin bundles, Current Biology (2025), https://doi.org/10.1016/j.cub.2025.10.081

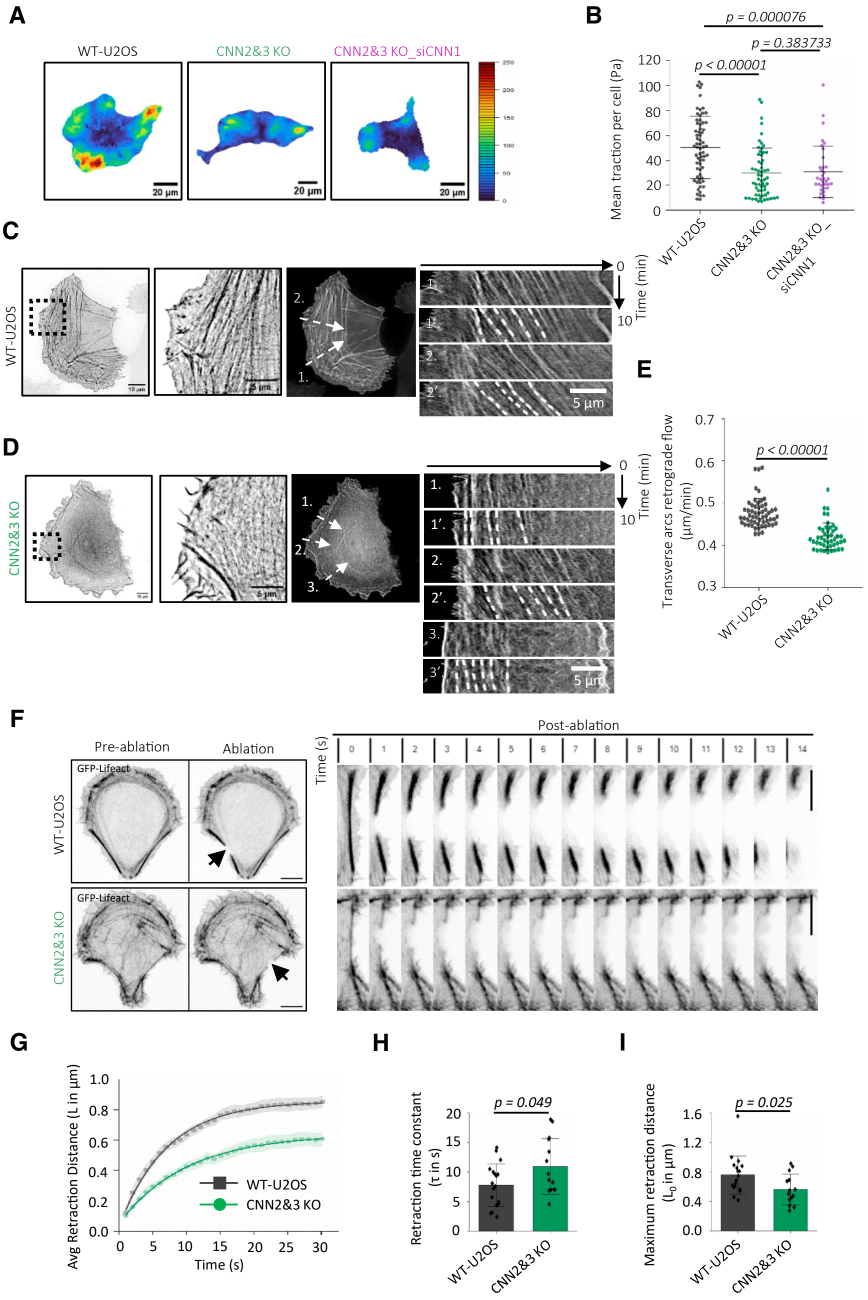

Figure 4. Effects of calponin depletions on myosin II-based contractility

(A) Representative traction force maps of wild-type, CNN2&3 KO, and CNN2&3 KO_siCNN1 cells plated on ~10 kPa hydrogels covered with 488 fluorescent nanobeads and coated with fibronectin. The color scale indicates traction forces from 0 to 250 Pascal (Pa). Scale bars, 20 µm.

(B) Quantification of mean tractions of wild-type (n = 66), CNN2&3 KO (n = 59), and CNN2&3 KO_siCNN1 (n = 35) cells. Data are mean ± SD from four experiments.

(C and D) Representative time-lapse images and kymographs from live-cell imaging analysis to measure the retrograde flow of transverse arcs in wild-type (C) and CNN2&3 KO (D) cells. Black dashed boxes in the whole-cell images indicate the magnified regions from the cell edge. The whole-cell images with white arrows numbered 1, 2, and 3 indicate the line regions of interest (ROIs) for the kymographs shown on the right. The white dashed lines in the 1′, 2′, and 3′ kymographs, corresponding to kymograph images 1, 2, and 3, highlight the retrograde flow of arcs during a 10 min imaging period. Scale bars, 10 and 5 µm, respectively.

(E) Transverse arc retrograde flow rate (µm/min) in wild-type and CNN2&3 KO cells. Data represent mean ± SEM of n = 127 line scans from 9 wild-type cells and 116 line scans from 5 CNN2&3 KO cells.

(F) Representative images of laser ablation of ventral SF (VSF) visualized in GFP-Lifeact-expressing wild-type and CNN2&3 KO U2OS cells seeded on crossbow micropatterns. The black arrowheads in the "ablation" panels highlight the region of VSF ablated, and the magnified images on the right show the retracting ends of the VSF at different time points post-ablation. Magnified image at 0 s illustrates the VSF pre-ablation. Scale bars, 10 µm.

(G) Line plot analyses illustrating the retraction distance measurement over time in wild-type and CNN2&3 KO cells. The retraction distances (symbols) are fitted to the Kelvin-Voigt equation (solid lines) ($L(t) = L_0\left(1 - e^{-t/\tau}\right) + D_a$), where L_0 represents the maximum retraction distance, τ is the viscoelastic time constant, and D_a is the length of the SF destroyed during photoablation.

(H and I) (H) Viscoelastic time constant (τ) and (I) maximum retraction distance (L_0) for severed VSF in wild-type and CNN2&3 KO U2OS cells. The data represent mean value ± SD from n = 18 (wild-type) and n = 14 (CNN2&3 KO) cells from three independent experiments. Statistical analysis by unpaired t test with Welch's correction.

See also Figure S4.

micropatterns. Also, these experiments, where we ablated ventral stress fibers, revealed decreased, rather than increased, contractility of actomyosin bundles in CNN2&3 double-knockout cells (Figures 4F–4I). Finally, our experiments revealed that caldesmon localized normally to stress fibers also in the CNN2&3 double-knockout cells, and FRAP experiments demonstrated that the dynamics of GFP-L-caldesmon in stress fibers were unaffected in the CNN3 or CNN2&3 double-knockout cells (Figures S3E–S3I). Together, these experiments provide evidence that calponins do not function as negative regulators of actomyosin contractility in cells and that they also do not control the localization or dynamics of caldesmon in non-muscle cells.

Calponins control α-actinin distribution and dynamics in actomyosin bundles

Because CNN1 was reported to enhance filament bundling *in vitro* together with α-actinin,[51] and because CNN3 co-localizes with α-actinin in stress fibers,[33] we next analyzed the effects of calponin depletion on the distribution and dynamics of α-actinin along stress fibers. Super-resolution 3D-structured illumination

Please cite this article in press as: Kokate et al., Calponin isoforms define the cell-type-specific organization and dynamics of actomyosin bundles, Current Biology (2025), https://doi.org/10.1016/j.cub.2025.10.081

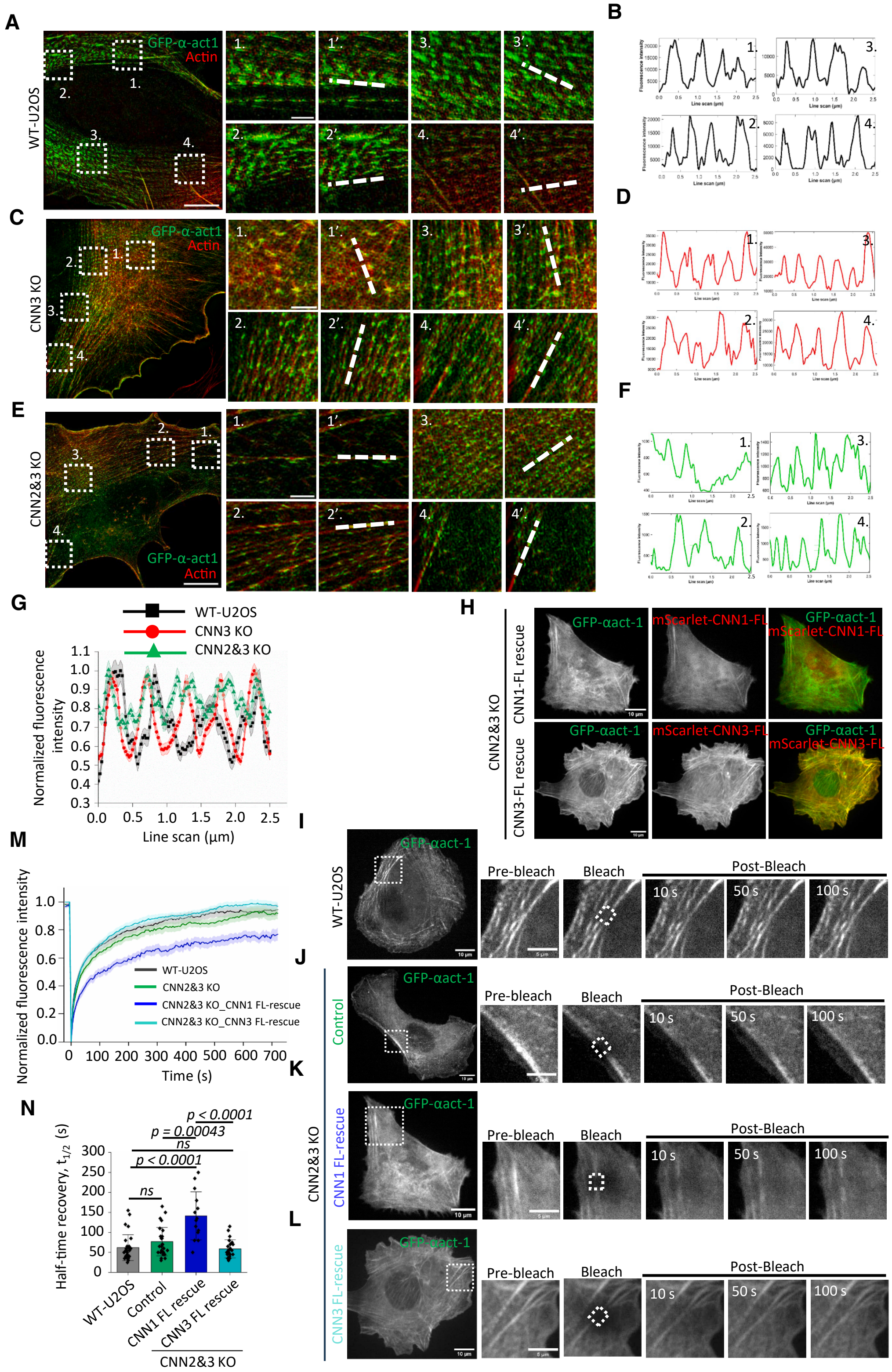

Figure 5. Calponins control the distribution and dynamics of α-actinin

(A, C, and E) Representative 3D-SIM images of (A) wild-type, (C) CNN3 KO, and (E) CNN2&3 KO U2OS cells expressing GFP-α-actinin-1 and with F-actin visualized by phalloidin staining. The panels on the right show magnified images indicated by white dashed boxes in the whole-cell images on the left.

(legend continued on next page)

microscopy (SIM) analysis demonstrated that GFP-α-actinin displayed relatively uniform periodic distribution along ventral stress fibers in different non-muscle-cell types (Figures 5A, 5B, and S5A–S5D). In the CNN3 knockout U2OS cells, this periodic pattern was evident in most regions, although some segments of ventral stress fibers displayed less regular distribution of α-actinin foci (Figures 5C and 5D). Importantly, regular periodic α-actinin distribution was nearly completely lost in the CNN2&3 double-knockout cells (Figures 5E and 5F). Moreover, line-scan analysis revealed that in wild-type cells the spacing between α-actinin foci in ventral stress fibers was ∼0.6 μm, whereas in the CNN3 knockout cells the average distances between α-actinin foci were ∼0.4 μm. Due to irregular α-actinin distribution, the spacing between α-actinin foci along the stress fibers could not be reliably measured from the CNN2&3 double-knockout cells (Figure 5G). Also, the regular distributions of myosin IIa and tropomyosins (Tpm1.6 and Tpm4.2) were compromised in the CNN2&3 double-knockout cells, but these defects appeared somewhat less severe as compared with the defects in distribution of the α-actinin foci (Figures S5E, S5F, and S6A–S6H).

α-Actinin displays dynamic association with stress fibers.[6] Although the periodic distribution of α-actinin along the stress fibers was severely defective in the CNN2&3 double-knockout cells, our FRAP experiments on cells expressing GFP-α-actinin provided evidence that the simultaneous depletion of CNN2 and CNN3 did not result in drastic effects on α-actinin dynamics in stress fibers (Figures 5H–5J, 5M, and 5N). Interestingly, whereas expression of CNN3 in the double-knockout cells did not significantly affect the dynamics of α-actinin, expression of the smooth-muscle isoform CNN1 resulted in ∼2.5-fold slower dynamics of α-actinin in stress fibers in the double-knockout cells (Figures 5H and 5K–5N). Moreover, similar experiments carried out on wild-type cells demonstrated that overexpression of CNN3 and CNN1 resulted in approximately 2- and 4-fold decreases in the recovery half-life of α-actinin in stress fibers, respectively (Figures S7A–S7D). Although the α-actinin dynamics along stress fibers were significantly affected by expression of CNN1, the dynamics of tropomyosins (Tpm1.6 and Tpm4.2), which are also central components of ventral stress fibers,[15] were largely unaffected by the expression of CNN1 in the CNN2&3 double-knockout cells (Figures S6I–S6P). Together, these results demonstrate that calponins are important components for proper molecular architecture of stress fibers by regulating the distribution of α-actinin foci along stress fibers. Moreover, these data suggest that calponins, especially CNN1, can also regulate the dynamics of α-actinin in stress fibers.

Calponin isoforms display different dynamics in stress fibers

When analyzing the different CNN2&3 double-knockout clones, we discovered that they expressed highly variable levels of the remaining "smooth-muscle" calponin isoform, CNN1. In the clone used in the studies described so far (clone G3 CL1), the protein levels of CNN1 were comparable to the one in the wild-type cells, but other clones, especially the clone "G1 CL5," expressed much higher (∼10-fold) levels of CNN1 (Figures S1K and S1L). Thus, this clone was named as "CNN2&3 KO_CNN1-high." Interestingly, the CNN2&3 KO_CNN1-high cells were larger as compared with the CNN2&3 knockout cells expressing normal levels of CNN1 and also appeared slightly more elongated (Figures S1M and S1N). Moreover, the stress fibers appeared thicker in the CNN2&3 KO_CNN1-high cells as compared with the CNN2&3 knockout clone expressing normal levels of CNN1 (Figures S1O–S1S). These data, together with the results described in the previous chapter, suggest that the "smooth-muscle calponin," CNN1, can stabilize α-actinin in stress fibers more efficiently as compared with "non-muscle calponin," CNN3, and that CNN1 and CNN3 have different effects on stress fiber organization and cell morphogenesis. This led us to examine the differences between these isoforms.

CNN3 exhibits rapid association-dissociation kinetics in stress fibers.[33] Interestingly, FRAP experiments revealed that EGFP-CNN1 displays >10-fold slower dynamics in ventral stress fibers of U2OS cells as compared with CNN3 (Figure 6). The key difference between CNN1 and CNN3 is the presence of an acidic (Glu/Asp-rich) C-terminal extension in CNN3 (Figure 6A). Thus, we also generated a C-terminally truncated version of CNN3 (CNN3ΔTail) comprising residues 1–273 and lacking the acidic C-terminal extension that is not present in CNN1 (Figure 6A). Importantly, the CNN3ΔTail displayed drastically decreased dynamics in stress fibers compared with the full-length CNN3 and exhibited a mean half-time recovery close to that of CNN1 (∼200 s vs. ∼300 s). Together, these results reveal that CNN3 exhibits rapid dynamics in stress fibers, whereas CNN1 is a relatively stable component of stress fibers. The difference between CNN1 and CNN3 is mainly due to the presence of an acidic C-terminal extension in CNN3.

Smooth-muscle and non-muscle calponins control the dynamics and architecture of actomyosin bundles in an isoform-specific manner

To directly examine the possible functional differences between CNN1 and CNN3, we carried out rescue experiments by using

(B, D, and F) The white dashed lines in the magnified images 1′–4′ represent the SF segments used for the line scan analyses shown in (B) for wild-type, (D) for CNN3 KO, and (F) for CNN2&3 KO cells. Scale bars, 5 and 1 μm for whole-cell and magnified images, respectively.

(G) Line plot analysis representing the mean distances between α-actinin-1 foci. Data are mean ± SEM of 22 line scans from 6 wild-type cells, 37 line scans from 5 CNN3 KO cells, and 36 line scans from 5 CNN2&3 KO cells.

(H) Representative images of CNN2&3 KO cells expressing GFP-α-actinin-1 and mScarlet-CNN1 or mScarlet-CNN3. Scale bar, 10 μm.

(I–L) FRAP analysis of GFP-α-actinin-1 dynamics in wild-type, CNN2&3 KO, and CNN1- and CNN3-rescued CNN2&3 KO cells. The white dashed boxes in the whole-cell images highlight the cell region shown in the time-lapse images, and the white dashed boxes in the second time-lapse images indicate the photobleached SF regions. Scale bars, 10 and 5 μm, respectively.

(M and N) (M) The recovery curves and (N) the recovery half-times of GFP-α-actinin-1 in wild-type, CNN2&3 KO, and CNN1-/CNN3-rescued KO cells. Line plots in (M) indicate mean ± SEM from *n* = 31 (wild-type), 27 (CNN2&3 KO), 13 (CNN2&3 KO_CNN1 rescue), and 22 (CNN2&3 KO_CNN3 rescue) cells.

See also Figures S5–S7.

Please cite this article in press as: Kokate et al., Calponin isoforms define the cell-type-specific organization and dynamics of actomyosin bundles, Current Biology (2025), https://doi.org/10.1016/j.cub.2025.10.081

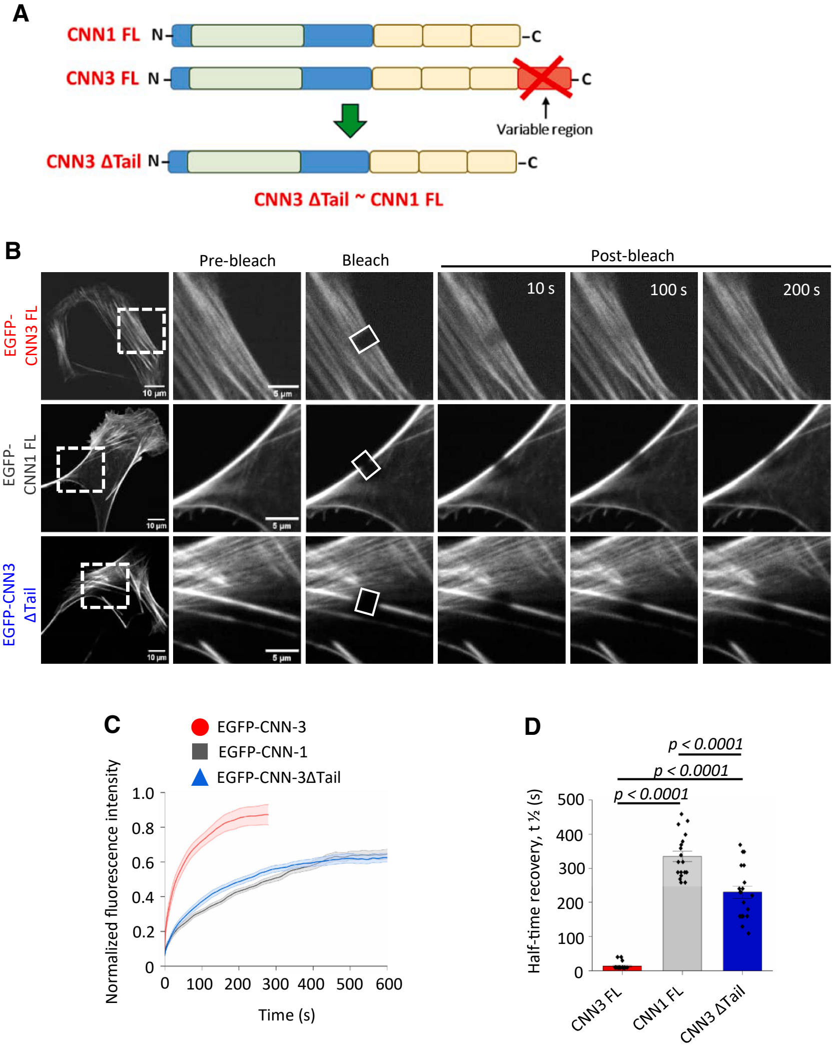

Figure 6. Smooth-muscle and non-muscle calponins display different dynamics in SFs

(A) Domain organizations of CNN1 and CNN3. The CH domains are in green, the CLIK repeats in yellow, and the C-terminal acidic tail, which is only present in CNN3, is in red. In the CNN3ΔTail construct, the C-terminal acidic tail was removed.

(B) Representative time-lapse frames from the FRAP experiments to study the dynamics of EGFP-CNN3 FL (full-length), EGFP-CNN-1 FL, and EGFP-CNN3ΔTail in wild-type U2OS cells. The white dashed boxes in the whole-cell images highlight the cell regions presented in the zoomed images, and the white boxes in the second time-lapse images show the photobleached regions. Scale bars, 10 and 5 μm, respectively.

(C and D) (C) The recovery curves and (D) the recovery half-times of EGFP-CNN3 FL, EGFP-CNN1 FL, and EGFP-CNN3ΔTail demonstrate that CNN3 is a highly dynamic component of SFs, whereas CNN1 and CNN3ΔTail display more stable association to SFs. Line plots indicate mean ± SEM from n = 16 (EGFP-CNN3 FL), 18 (EGFP-CNN1 FL), and 17 (EGFP-CNN3ΔTail) photobleaching experiments. The experiments were repeated three times.

the CNN2&3 double-knockout clone expressing “normal” levels of CNN1 (G3 CL1, generated by using guide 3 RNA). Importantly, these knockout-rescue experiments revealed drastic differences in the stress fiber phenotypes: although automated stress fiber analysis did not detect statistically significant differences in the average thickness of stress fibers between CNN1- and CNN3-rescue cells (Figure S2K), blind analysis provided evidence that there were more thick and better aligned stress fibers in the CNN1-rescue cells as compared with the CNN3-rescue cells (Figures 7A–7C, S7E, and S7F). Moreover, the CNN1 and CNN3ΔTail rescue cells were larger in area and more elongated as compared with the CNN3-rescue cells (Figures 7D and 7E). Expression of CNN3 also partially rescued the cell migration phenotype of the CNN2&3 double-knockout cells, whereas the CNN1 and CNN3ΔTail “rescue” cells were even less motile than the CNN2&3 double-knockout cells (Figures 7F and 7G). Finally, we compared the dynamics of stress fibers in different rescue cells. As described in a previous chapter, transverse arcs undergo retrograde flow at cell edges, and this was diminished in the CNN2&3 double-knockout cells. The slower velocity of arcs could be partially rescued by expression of full-length CNN3 in the CNN2&3 double-knockout cells. However, in the CNN1 and CNN3ΔTail expressing CNN2&3 double cells, stress fibers were typically very thick and immobile, and these abnormally thick stress fibers close to the cell edge underwent slower retrograde flow as compared with the transverse arcs that were present close to the cell edges of wild-type and CNN3-rescue cells (Figures S7G–S7K). Moreover, laser-ablation experiments provided evidence that the thick stress fibers induced upon overexpression of CNN1 in wild-type cells displayed decreased maximum retraction distances as compared with wild-type “control” cells. These results show that the expression of smooth-muscle CNN1 in non-muscle cells does not increase, but rather decreases, the contractility of individual stress fibers (Figures S7L–S7O). Collectively, these experiments provide evidence that non-muscle CNN3 displays rapid turnover in stress fibers and allows their dynamic remodeling. On the other hand, the smooth-muscle isoform, CNN1, displays stable association with stress fibers and hence promotes the formation of thicker, static, and less contractile stress fibers, which promote cell elongation and inhibit cell migration.

DISCUSSION

Despite their identification nearly four decades ago,[20] the precise cellular roles of calponin family proteins have remained elusive. This may be partly due to the presence of three highly homologous calponin isoforms in vertebrates. By analyzing non-muscle cells lacking either individual, two, or all three calponin isoforms, we provide evidence that these proteins exhibit partially redundant functions with each other in cell migration, invasion, and actomyosin organization. However, as discussed

Please cite this article in press as: Kokate et al., Calponin isoforms define the cell-type-specific organization and dynamics of actomyosin bundles, Current Biology (2025), https://doi.org/10.1016/j.cub.2025.10.081

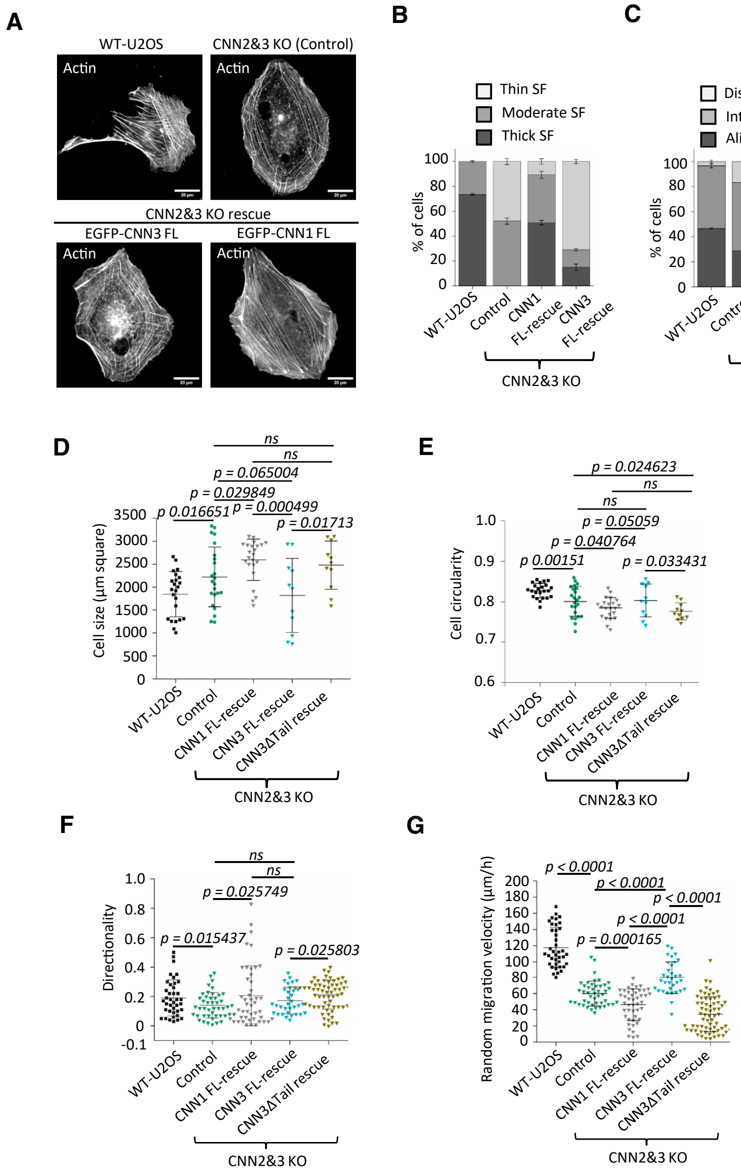

Figure 7. Isoform-specific effects of calponins on cell morphogenesis, migration, and SF organization

(A) Representative fluorescence microscopy images of wild-type cells, as well as CNN2&3 KO cells (same examples as in Figure 2), rescued with EGFP-CNN1 and EGFP-CNN3 plasmids. Actin filaments were visualized with fluorescent phalloidin. Scale bars, 10 µm.

(B) Blind analysis of the percentage of thin, intermediate, and thick SFs in wild-type (n = 30), CNN2&3 KO (n = 31), CNN2&3 KO-CNN1 rescue (n = 26), and CNN2&3 KO-CNN3 rescue (n = 28) cells. The error bars represent mean ± SEM.

(C) Blind analysis of the percentage of cells having disorganized, intermediate, and aligned SFs in wild-type (n = 30), CNN2&3 KO (n = 31), CNN2&3 KO-CNN1 rescue (n = 26), and CNN2&3 KO-CNN3 rescue (n = 28) cells. The error bars represent mean ± SEM.

(D and E) (D) Graphical representations of cell size and (E) cell shape analyses performed for wild-type, CNN2&3 KO, and KO-rescue cells. Data represent mean ± SD of n = 5,421 (wild-type), 6,131 (CNN2&3 KO), 16,529 (CNN2&3 KO-CNN1 rescue), 2,190 (CNN2&3 KO_CNN3 rescue), and 2,632 (CNN2&3 KO_CNN3ΔTail rescue) cells. Each data point in the graphs represents the mean value of a single well from a 96-well plate.

(F and G) (F) Graphical representation of cell directionality and (G) random migration velocity analyses. Data represent mean ± SEM of n = 39 (wild-type), 45 (CNN2&3 KO), 45 (CNN2&3 KO-CNN1 FL-rescue), 33 (CNN2&3 KO-CNN3 FL-rescue), and 66 (CNN2&3 KO-CNN3ΔTail-rescue) cells.

See also Figures S2 and S7.

below, the smooth-muscle (CNN1) and the ubiquitous non-muscle (CNN3) calponins display different dynamics, which manifests as distinct properties of the actomyosin bundles they associate with.

Previous biochemical studies proposed that calponins function as negative regulators of actin-activated myosin II ATPase in smooth-muscle and non-muscle cells.[26,48,49,52,53] However, several lines of evidence from this study suggest that at least in non-muscle cells calponins do not function as negative regulators of actomyosin contractility. This is because (1) CNN2&3 double-knockout cells and CNN1-silenced double-knockout cells exhibited decreased, not increased, traction forces; (2) retrograde flow of transverse arcs, which is a process powered by myosin II, was slower in the CNN2&3 double-knockout cells as compared with wild-type cells; (3) laser-ablation experiments provided evidence that individual ventral stress fibers are less contractile in the CNN2&3 double-knockout cells; (4) the stress fibers were thinner in the calponin-depleted cells, whereas increased actomyosin contractility would be expected to lead to reinforcement of stress fibers[54]; and (5) CNN3 does not co-localize with myosin II in stress fibers, but instead accumulates at α-actinin-rich foci along stress fibers.[33] Moreover, the increased dynamics of myosin IIb in stress fibers of CNN2&3 double-knockout cells may also result from their decreased contractility, because an earlier study linked slower turnover of myosin II to increased cortical tension during mitosis.[55] Our results are also consistent with earlier studies on CNN1 and CNN1/CNN2 knockout mice, which demonstrated that loss of these calponins resulted in rather modest effects on smooth-muscle contractility.[28,56] Thus, we propose that, although calponins can inhibit myosin II/actin interaction in biochemical experiments, most likely due to partially overlapping binding sites of myosin II and calponin on an actin filament, these two proteins localize to different regions of actomyosin bundles, and hence calponins do not control myosin II activity in cells. It is also important to note that previous studies, where individual calponin isoforms were depleted, led to controversial results on the roles of calponins in actomyosin contractility.[33–35] Because our study demonstrated that different

Please cite this article in press as: Kokate et al., Calponin isoforms define the cell-type-specific organization and dynamics of actomyosin bundles, Current Biology (2025), https://doi.org/10.1016/j.cub.2025.10.081

calponin isoforms have partially overlapping cellular functions but slightly different effects on stress fiber dynamics, the possible roles of calponins in actomyosin contractility were important to examine in cells where all three calponin isoforms were simultaneously depleted. Moreover, calponins are also unlikely to regulate actomyosin contractility through caldesmon as proposed in an earlier study.[36] This is because caldesmon localization and dynamics were unaffected in CNN3 and CNN2&3 depleted cells, and our recent study revealed that caldesmon is not a negative regulator of actomyosin contractility in cells as suggested by earlier biochemical studies.[18] Thus, we propose that any protein with an overlapping binding site on actin can inhibit the actin-stimulated ATPase activity of myosin II to some extent *in vitro*, but this does not mean that these proteins would function as regulators of actomyosin contractility in a more complex cellular context.

Although calponins do not appear to function as negative regulators of actomyosin contractility, our results reveal that they are important regulators of stress fiber architecture. Whilst individual depletions of CNN2 and CNN3 did not display prominent defects in stress fibers, stress fibers in the CNN2&3 double-knockout cells and especially in the cells lacking all three calponins were very thin and fragile. Our results also revealed that calponins can control the localization and dynamics of a central actin filament cross-linking protein, α-actinin, in stress fibers (Figure S7P). This is because the regular, periodic distribution of α-actinin along stress fibers was lost in the CNN2&3 double-knockout cells, and because overexpression of CNN1 diminished the dynamics of α-actinin in stress fibers. Therefore, we propose that calponins function together with α-actinin to cross-link actin filaments in higher-order structures in stress fibers. This notion is also in agreement with an earlier biochemical study suggesting that calponins interact directly with α-actinin to enhance actin filament bundling *in vitro*, although the underlying structural mechanism is currently not known.[51] In the absence of calponins and regular distribution of α-actinin, also other components of stress fibers, many of which do not co-localize with α-actinin and calponins (e.g., myosin II and some tropomyosin isoforms), display abnormal distribution along the remaining thin stress fibers. These architectural problems in stress fibers are expected to result in their decreased contractility and accompanied abnormalities in cell morphogenesis, migration, and invasion.

Our work also revealed key differences between non-muscle CNN3 and smooth-muscle CNN1 that correlate with their roles in assembling specific actomyosin bundles. Non-muscle CNN3 displays rapid turnover in stress fibers and allows their dynamic remodeling. On the other hand, the smooth-muscle CNN1 displays a much more stable association with stress fibers and stabilizes α-actinin in stress fibers. Consequently, CNN1 induces the formation of thicker, better-aligned, and more static stress fibers, which resemble the actomyosin bundles of smooth-muscle cells.[3,57] However, despite increased thickness, the abnormally thick actomyosin bundles induced by overexpression of CNN1 are not more contractile, suggesting that their architecture or dynamics are not optimal for non-muscle II isoforms. Our results also demonstrate that the main functional difference between these calponin isoforms is the presence of an acidic C-terminal tail in CNN3, because its deletion led to CNN1-like dynamics, as well as appearance of static stress fibers and inhibition of cell migration (Figure S7P). These latter results are also in line with an earlier work providing evidence that removal of the C-terminal tail from CNN2 resulted in more prominent localization of the mutant calponin to stress fibers and in the appearance of thicker stress fibers.[32] Thus, we propose that, in addition to the presence of smooth-muscle-specific actin and myosin II isoforms, a major difference between non-muscle cell stress fibers and smooth-muscle actomyosin bundles is the presence of "stable" CNN1, which organizes actin filaments into thicker and more stable bundles in smooth muscles. This is due to the lack of an acidic C-terminal region, which in non-muscle CNN2 and CNN3 is responsible for their highly dynamic interactions with actomyosin bundles.

Differences between calponin isoforms observed here may also elucidate their roles in cancer progression. CNN2 and CNN3 were reported to be upregulated in several cancers, including lung, urothelial, cervical, and endothelial cancers, as well as in gliomas and glioblastomas. On the other hand, CNN1 is rarely upregulated in cancers.[58–60] This distinction could be linked to the ability of the cancer-associated CNN2 and CNN3 to induce dynamic actomyosin bundles supportive of migration and invasion of cancer cells, whereas the stable actomyosin bundles induced by CNN1 would inhibit cancer cell motility. This hypothesis is also supported by our data demonstrating that depletion of CNN2 and CNN3 resulted in defects in cell migration and invasion, as well as by the present and earlier data demonstrating that overexpression of CNN1 inhibits cell migration.[61] In the future, it will be important to uncover the precise mechanism by which calponins, together with α-actinin, regulate stress fiber architecture and to reveal the molecular mechanism by which the acidic C-terminal tails of non-muscle CNN2 and CNN3 increase their dynamics in stress fibers.

RESOURCE AVAILABILITY

Lead contact

Requests for further information and resources should be directed to and will be fulfilled by the lead contact, Pekka Lappalainen (pekka.lappalainen@helsinki.fi).

Materials availability

All calponin knockout cell lines and other reagents generated in this study will be made available from the lead contact upon reasonable request.

Data and code availability

- All data needed to evaluate the conclusions of the publication are presented in the paper and in the supplemental information. The raw, original files related to the study can be obtained from the lead contact upon reasonable request.
- This paper does not report original code.
- Any additional information required to reanalyze the data reported in this paper is available from the lead contact upon request.

ACKNOWLEDGMENTS

We thank the staff at the Institute of Biotechnology Light Microscopy Unit (LMU), Biomedicum Imaging Unit (BIU), and Quantitative Chemically-Specific Imaging Infrastructure for Material and Life Sciences (qCSI) facilities of the University of Helsinki for technical advice and support during microscopy and image analysis. We would especially like to thank Mikko Liljeström and Antti Isomäki from the BIU for their extensive assistance during the manuscript revision experiments. For services, instrumentation, and expertise, we would like to thank the Cell Imaging and Cytometry Core (Turku Bioscience Centre, University of Turku), supported by Biocenter Finland, and the Euro-BioImaging Finnish Node (Turku, Finland). We are grateful to Leo Almeida-Souza (HiLIFE-BI, University of Helsinki, Finland) for the generous gift of NIH/3T3 cells used in the super-resolution imaging experiments. We also thank Mirva Tirkkonen, Petra Laasola, and Jenni Siivonen for technical assistance. This work was supported by the Academy of Finland (Center of Excellence grants 346133 and 346131 to P.L. and J.I., respectively; research fellowship 343239 to M.C.; and InFLAMES Flagship Programme 337530 to J.I.), the Sigrid Juselius Foundation (4708344 to P.L.), and the Finnish Cancer Institute (K. Albin Johansson Professorship to J.I.).

AUTHOR CONTRIBUTIONS

S.B.K. and P.L. crafted the original idea and initiated the study. S.B.K. designed and performed the majority of the experiments and analyzed and interpreted the results. A.T.O. performed CNN1 silencing and analysis of SFs and focal adhesions. M.C. performed TFM experiments. X.L.C. and P.B. helped in the experimental and analysis part. K.K. contributed to cloning. T.T. helped in the laser-ablation experiments. P.L. and J.I. procured funding for this project. S.B.K. and P.L. wrote the manuscript with input from other authors.

DECLARATION OF INTERESTS

The authors declare no competing interests.

STAR★METHODS

Detailed methods are provided in the online version of this paper and include the following:

- KEY RESOURCES TABLE
- EXPERIMENTAL MODEL AND SUBJECT DETAILS
    - Cell-lines and transfections
- METHOD DETAILS
    - Plasmids
    - Generation of knockout cell-lines
    - siRNA experiments
    - Micropatterns
    - Immunofluorescence stainings
    - Fluorescence-recovery-after-photobleaching (FRAP)
    - Traction force microscopy
    - Fixed-cell imaging
    - Live-cell imaging
    - Wide-field imaging
    - 3D-SIM super-resolution imaging
    - Laser ablation
    - Wound healing assay
    - Random cell migration assay
    - High-content imaging
    - *In-vitro* transwell invasion assay
    - Western blotting
    - Image analysis
- QUANTIFICATION AND STATISTICAL ANALYSIS

SUPPLEMENTAL INFORMATION

Supplemental information can be found online at https://doi.org/10.1016/j.cub.2025.10.081.

Received: April 24, 2025
Revised: September 18, 2025
Accepted: October 29, 2025

REFERENCES

1. Tojkander, S., Gateva, G., and Lappalainen, P. (2012). Actin stress fibers–assembly, dynamics and biological roles. J. Cell Sci. *125*, 1855–1864. https://doi.org/10.1242/jcs.098087.
2. Prager-Khoutorsky, M., Lichtenstein, A., Krishnan, R., Rajendran, K., Mayo, A., Kam, Z., Geiger, B., and Bershadsky, A.D. (2011). Fibroblast polarization is a matrix-rigidity-dependent process controlled by focal adhesion mechanosensing. Nat. Cell Biol. *13*, 1457–1465. https://doi.org/10.1038/ncb2370.
3. Livne, A., and Geiger, B. (2016). The inner workings of stress fibers - from contractile machinery to focal adhesions and back. J. Cell Sci. *129*, 1293–1304. https://doi.org/10.1242/jcs.180927.
4. Engler, A.J., Sen, S., Sweeney, H.L., and Discher, D.E. (2006). Matrix elasticity directs stem cell lineage specification. Cell *126*, 677–689. https://doi.org/10.1016/j.cell.2006.06.044.
5. Fenix, A.M., Neininger, A.C., Taneja, N., Hyde, K., Visetsouk, M.R., Garde, R.J., Liu, B., Nixon, B.R., Manalo, A.E., Becker, J.R., et al. (2018). Muscle-specific stress fibers give rise to sarcomeres in cardiomyocytes. eLife *7*, e42144. https://doi.org/10.7554/eLife.42144.
6. Hotulainen, P., and Lappalainen, P. (2006). Stress fibers are generated by two distinct actin assembly mechanisms in motile cells. J. Cell Biol. *173*, 383–394. https://doi.org/10.1083/jcb.200511093.
7. Lee, S., and Kumar, S. (2016). Actomyosin stress fiber mechanosensing in 2D and 3D. F1000Res *5*, F1000FacultyRev-2261. https://doi.org/10.12688/f1000research.8800.1.
8. Shutova, M.S., Asokan, S.B., Talwar, S., Assoian, R.K., Bear, J.E., and Svitkina, T.M. (2017). Self-sorting of nonmuscle myosins IIA and IIB polarizes the cytoskeleton and modulates cell motility. J. Cell Biol. *216*, 2877–2889. https://doi.org/10.1083/jcb.201705167.
9. Tojkander, S., Gateva, G., Husain, A., Krishnan, R., and Lappalainen, P. (2015). Generation of contractile actomyosin bundles depends on mechanosensitive actin filament assembly and disassembly. eLife *4*, e06126. https://doi.org/10.7554/eLife.06126.
10. Gateva, G., Tojkander, S., Koho, S., Carpen, O., and Lappalainen, P. (2014). Palladin promotes assembly of non-contractile dorsal stress fibers through VASP recruitment. J. Cell Sci. *127*, 1887–1898. https://doi.org/10.1242/jcs.135780.
11. Kumari, R., Jiu, Y., Carman, P.J., Tojkander, S., Kogan, K., Varjosalo, M., Gunning, P.W., Dominguez, R., and Lappalainen, P. (2020). Tropomodulins control the balance between protrusive and contractile structures by stabilizing actin-tropomyosin filaments. Curr. Biol. *30*, 767–778.e5. https://doi.org/10.1016/j.cub.2019.12.049.
12. Phua, D.Y.Z., Sun, X., and Alushin, G.M. (2025). Force-activated zyxin assemblies coordinate actin nucleation and crosslinking to orchestrate stress fiber repair. Curr. Biol. *35*, 854–870.e9. https://doi.org/10.1016/j.cub.2025.01.042.
13. Schulze, N., Graessl, M., Blancke Soares, A., Geyer, M., Dehmelt, L., and Nalbant, P. (2014). FHOD1 regulates stress fiber organization by controlling the dynamics of transverse arcs and dorsal fibers. J. Cell Sci. *127*, 1379–1393. https://doi.org/10.1242/jcs.134627.
14. Smith, M.A., Blankman, E., Gardel, M.L., Luettjohann, L., Waterman, C.M., and Beckerle, M.C. (2010). A zyxin-mediated mechanism for actin stress fiber maintenance and repair. Dev. Cell *19*, 365–376. https://doi.org/10.1016/j.devcel.2010.08.008.
15. Tojkander, S., Gateva, G., Schevzov, G., Hotulainen, P., Naumanen, P., Martin, C., Gunning, P.W., and Lappalainen, P. (2011). A molecular pathway for myosin II recruitment to stress fibers. Curr. Biol. *21*, 539–550. https://doi.org/10.1016/j.cub.2011.03.007.
16. Winkelman, J.D., Anderson, C.A., Suarez, C., Kovar, D.R., and Gardel, M.L. (2020). Evolutionarily diverse LIM domain-containing proteins bind stressed actin filaments through a conserved mechanism. Proc. Natl. Acad. Sci. USA *117*, 25532–25542. https://doi.org/10.1073/pnas.2004656117.

17. Jiu, Y., Kumari, R., Fenix, A.M., Schaible, N., Liu, X., Varjosalo, M., Krishnan, R., Burnette, D.T., and Lappalainen, P. (2019). Myosin-18B promotes the assembly of myosin II stacks for maturation of contractile actomyosin bundles. Curr. Biol. *29*, 81–92.e5. https://doi.org/10.1016/j.cub.2018.11.045.

18. Kokate, S.B., Ciuba, K., Tran, V.D., Kumari, R., Tojkander, S., Engel, U., Kogan, K., Kumar, S., and Lappalainen, P. (2022). Caldesmon controls stress fiber force-balance through dynamic cross-linking of myosin II and actin-tropomyosin filaments. Nat. Commun. *13*, 6032. https://doi.org/10.1038/s41467-022-33688-w.

19. Lehtimäki, J.I., Fenix, A.M., Kotila, T.M., Balistreri, G., Paavolainen, L., Varjosalo, M., Burnette, D.T., and Lappalainen, P. (2017). UNC-45a promotes myosin folding and stress fiber assembly. J. Cell Biol. *216*, 4053–4072. https://doi.org/10.1083/jcb.201703107.

20. Takahashi, K., Hiwada, K., and Kokubu, T. (1986). Isolation and characterization of a 34000-dalton calmodulin- and F-actin-binding protein from chicken gizzard smooth muscle. Biochem. Biophys. Res. Commun. *141*, 20–26. https://doi.org/10.1016/s0006-291x(86)80328-x.

21. Hsieh, T.B., and Jin, J.P. (2023). Evolution and function of calponin and transgelin. Front. Cell Dev. Biol. *11*, 1206147. https://doi.org/10.3389/fcell.2023.1206147.

22. Winder, S.J., and Walsh, M.P. (1990). Smooth muscle calponin. Inhibition of actomyosin MgATPase and regulation by phosphorylation. J. Biol. Chem. *265*, 10148–10155. https://doi.org/10.1016/S0021-9258(19)38792-7.

23. Liu, R., and Jin, J.P. (2016). Calponin isoforms CNN1, CNN2 and CNN3: Regulators for actin cytoskeleton functions in smooth muscle and non-muscle cells. Gene *585*, 143–153. https://doi.org/10.1016/j.gene.2016.02.040.

24. Ono, S. (2021). Diversification of the calponin family proteins by gene amplification and repeat expansion of calponin-like motifs. Cytoskeleton (Hoboken) *78*, 199–205. https://doi.org/10.1002/cm.21683.

25. Matthew, J.D., Khromov, A.S., McDuffie, M.J., Somlyo, A.V., Somlyo, A.P., Taniguchi, S., and Takahashi, K. (2000). Contractile properties and proteins of smooth muscles of a calponin knockout mouse. J. Physiol. *529*, 811–824. https://doi.org/10.1111/j.1469-7793.2000.00811.x.

26. Takahashi, K., Yoshimoto, R., Fuchibe, K., Fujishige, A., Mitsui-Saito, M., Hori, M., Ozaki, H., Yamamura, H., Awata, N., Taniguchi, S., et al. (2000). Regulation of shortening velocity by calponin in intact contracting smooth muscles. Biochem. Biophys. Res. Commun. *279*, 150–157. https://doi.org/10.1006/bbrc.2000.3909.

27. Facemire, C., Brozovich, F.V., and Jin, J.P. (2000). The maximal velocity of vascular smooth muscle shortening is independent of the expression of calponin. J. Muscle Res. Cell Motil. *21*, 367–373. https://doi.org/10.1023/a:1005680614296.

28. Nigam, R., Triggle, C.R., and Jin, J.P. (1998). h1- and h2-calponins are not essential for norepinephrine- or sodium fluoride-induced contraction of rat aortic smooth muscle. J. Muscle Res. Cell Motil. *19*, 695–703. https://doi.org/10.1023/a:1005389300151.

29. Huang, Q.Q., Hossain, M.M., Sun, W., Xing, L., Pope, R.M., and Jin, J.P. (2016). Deletion of calponin 2 in macrophages attenuates the severity of inflammatory arthritis in mice. Am. J. Physiol. Cell Physiol. *311*, C673–C685. https://doi.org/10.1152/ajpcell.00331.2015.

30. Huang, Q.Q., Hossain, M.M., Wu, K., Parai, K., Pope, R.M., and Jin, J.P. (2008). Role of H2-calponin in regulating macrophage motility and phagocytosis. J. Biol. Chem. *283*, 25887–25899. https://doi.org/10.1074/jbc.M801163200.

31. Junghans, D., and Herzog, S. (2018). Cnn3 regulates neural tube morphogenesis and neuronal stem cell properties. FEBS J. *285*, 325–338. https://doi.org/10.1111/febs.14338.

32. Burgstaller, G., Kranewitter, W.J., and Gimona, M. (2002). The molecular basis for the autoregulation of calponin by isoform-specific C-terminal tail sequences. J. Cell Sci. *115*, 2021–2029. https://doi.org/10.1242/jcs.115.10.2021.

33. Ciuba, K., Hawkes, W., Tojkander, S., Kogan, K., Engel, U., Iskratsch, T., and Lappalainen, P. (2018). Calponin-3 is critical for coordinated contractility of actin stress fibers. Sci. Rep. *8*, 17670. https://doi.org/10.1038/s41598-018-35948-6.

34. Daimon, E., Shibukawa, Y., and Wada, Y. (2013). Calponin 3 regulates stress fiber formation in dermal fibroblasts during wound healing. Arch. Dermatol. Res. *305*, 571–584. https://doi.org/10.1007/s00403-013-1343-8.

35. Hossain, M.M., Zhao, G., Woo, M.S., Wang, J.H.C., and Jin, J.P. (2016). Deletion of calponin 2 in mouse fibroblasts increases myosin II-dependent cell traction force. Biochemistry *55*, 6046–6055. https://doi.org/10.1021/acs.biochem.6b00856.

36. Appel, S., Allen, P.G., Vetterkind, S., Jin, J.P., and Morgan, K.G. (2010). h3/Acidic calponin: an actin-binding protein that controls extracellular signal-regulated kinase 1/2 activity in nonmuscle cells. Mol. Biol. Cell *21*, 1409–1422. https://doi.org/10.1091/mbc.e09-06-0451.

37. Flemming, A., Huang, Q.Q., Jin, J.P., Jumaa, H., and Herzog, S. (2015). A conditional knockout mouse model reveals that calponin-3 is dispensable for early B cell development. PLoS One *10*, e0128385. https://doi.org/10.1371/journal.pone.0128385.

38. Hines, P.C., Gao, X., White, J.C., D'Agostino, A., and Jin, J.P. (2014). A novel role of h2-calponin in regulating whole blood thrombosis and platelet adhesion during physiologic flow. Physiol. Rep. *2*, e12228. https://doi.org/10.14814/phy2.12228.

39. Hossain, M.M., Crish, J.F., Eckert, R.L., Lin, J.J.C., and Jin, J.P. (2005). h2-Calponin is regulated by mechanical tension and modifies the function of actin cytoskeleton. J. Biol. Chem. *280*, 42442–42453. https://doi.org/10.1074/jbc.M509952200.

40. Hossain, M.M., Smith, P.G., Wu, K., and Jin, J.P. (2006). Cytoskeletal tension regulates both expression and degradation of h2-calponin in lung alveolar cells. Biochemistry *45*, 15670–15683. https://doi.org/10.1021/bi061718f.

41. Jiang, W.R., Cady, G., Hossain, M.M., Huang, Q.Q., Wang, X., and Jin, J.P. (2014). Mechanoregulation of h2-calponin gene expression and the role of Notch signaling. J. Biol. Chem. *289*, 1617–1628. https://doi.org/10.1074/jbc.M113.498147.

42. Moazzem Hossain, M., Wang, X., Bergan, R.C., and Jin, J.P. (2014). Diminished expression of h2-calponin in prostate cancer cells promotes cell proliferation, migration and the dependence of cell adhesion on substrate stiffness. FEBS Open Bio *4*, 627–636. https://doi.org/10.1016/j.fob.2014.06.003.

43. Tang, J., Hu, G., Hanai, J., Yadlapalli, G., Lin, Y., Zhang, B., Galloway, J., Bahary, N., Sinha, S., Thisse, B., et al. (2006). A critical role for calponin 2 in vascular development. J. Biol. Chem. *281*, 6664–6672. https://doi.org/10.1074/jbc.M506991200.

44. Gimona, M., Kaverina, I., Resch, G.P., Vignal, E., and Burgstaller, G. (2003). Calponin repeats regulate actin filament stability and formation of podosomes in smooth muscle cells. Mol. Biol. Cell *14*, 2482–2491. https://doi.org/10.1091/mbc.e02-11-0743.

45. Jensen, M.H., Morris, E.J., Gallant, C.M., Morgan, K.G., Weitz, D.A., and Moore, J.R. (2014). Mechanism of calponin stabilization of cross-linked actin networks. Biophys. J. *106*, 793–800. https://doi.org/10.1016/j.bpj.2013.12.042.

46. Czuryło, E.A., Kulikova, N., and Dbrowska, R. (1997). Does calponin interact with caldesmon? J. Biol. Chem. *272*, 32067–32070. https://doi.org/10.1074/jbc.272.51.32067.

47. Graceffa, P., Adam, L.P., and Morgan, K.G. (1996). Strong interaction between caldesmon and calponin. J. Biol. Chem. *271*, 30336–30339. https://doi.org/10.1074/jbc.271.48.30336.

48. Kołakowski, J., Makuch, R., Stepkowski, D., and Dabrowska, R. (1995). Interaction of calponin with actin and its functional implications. Biochem. J. *306*, 199–204. https://doi.org/10.1042/bj3060199.

49. Winder, S.J., and Walsh, M.P. (1993). Calponin: thin filament-linked regulation of smooth muscle contraction. Cell. Signal. *5*, 677–686. https://doi.org/10.1016/0898-6568(93)90029-l.

50. Tee, Y.H., Shemesh, T., Thiagarajan, V., Hariadi, R.F., Anderson, K.L., Page, C., Volkmann, N., Hanein, D., Sivaramakrishnan, S., Kozlov, M.M., et al. (2015). Cellular chirality arising from the self-organization of the actin cytoskeleton. Nat. Cell Biol. *17*, 445–457. https://doi.org/10.1038/ncb3137.

51. Leinweber, B., Tang, J.X., Stafford, W.F., and Chalovich, J.M. (1999). Calponin interaction with alpha-actinin-actin: evidence for a structural role for calponin. Biophys. J. *77*, 3208–3217. https://doi.org/10.1016/S0006-3495(99)77151-1.

52. Ono, K., Obinata, T., Yamashiro, S., Liu, Z., and Ono, S. (2015). UNC-87 isoforms, Caenorhabditis elegans calponin-related proteins, interact with both actin and myosin and regulate actomyosin contractility. Mol. Biol. Cell *26*, 1687–1698. https://doi.org/10.1091/mbc.E14-10-1483.

53. Winder, S.J., Allen, B.G., Clément-Chomienne, O., and Walsh, M.P. (1998). Regulation of smooth muscle actin-myosin interaction and force by calponin. Acta Physiol. Scand. *164*, 415–426. https://doi.org/10.1111/j.1365-201x.1998.tb10697.x.

54. Burridge, K., and Wittchen, E.S. (2013). The tension mounts: stress fibers as force-generating mechanotransducers. J. Cell Biol. *200*, 9–19. https://doi.org/10.1083/jcb.201210090.

55. Taneja, N., Baillargeon, S.M., and Burnette, D.T. (2021). Myosin light chain kinase-driven myosin II turnover regulates actin cortex contractility during mitosis. Mol. Biol. Cell *32*, br3. https://doi.org/10.1091/mbc.E20-09-0608.

56. Feng, H.Z., Wang, H., Takahashi, K., and Jin, J.P. (2019). Double deletion of calponin 1 and calponin 2 in mice decreases systemic blood pressure with blunted length-tension response of aortic smooth muscle. J. Mol. Cell. Cardiol. *129*, 49–57. https://doi.org/10.1016/j.yjmcc.2019.01.026.

57. Small, J.V., and Gimona, M. (1998). The cytoskeleton of the vertebrate smooth muscle cell. Acta Physiol. Scand. *164*, 341–348. https://doi.org/10.1046/j.1365-201X.1998.00441.x.

58. Uhlén, M., Karlsson, M.J., Hober, A., Svensson, A.S., Scheffel, J., Kotol, D., Zhong, W., Tebani, A., Strandberg, L., Edfors, F., et al. (2019). The human secretome. Sci. Signal. *12*, eaaz0274. https://doi.org/10.1126/scisignal.aaz0274.

59. Uhlen, M., Zhang, C., Lee, S., Sjöstedt, E., Fagerberg, L., Bidkhori, G., Benfeitas, R., Arif, M., Liu, Z., Edfors, F., et al. (2017). A pathology atlas of the human cancer transcriptome. Science *357*, eaan2507. https://doi.org/10.1126/science.aan2507.

60. Tang, Z., Li, C., Kang, B., Gao, G., Li, C., and Zhang, Z. (2017). GEPIA: a web server for cancer and normal gene expression profiling and interactive analyses. Nucleic Acids Res. *45*, W98–W102. https://doi.org/10.1093/nar/gkx247.

61. Danninger, C., and Gimona, M. (2000). Live dynamics of GFP-calponin: isoform-specific modulation of the actin cytoskeleton and autoregulation by C-terminal sequences. J. Cell Sci. *113*, 3725–3736. https://doi.org/10.1242/jcs.113.21.3725.

62. Kumari, R., Ven, K., Chastney, M., Kokate, S.B., Peränen, J., Aaron, J., Kogan, K., Almeida-Souza, L., Kremneva, E., Poincloux, R., et al. (2024). Focal adhesions contain three specialized actin nanoscale layers. Nat. Commun. *15*, 2547. https://doi.org/10.1038/s41467-024-46868-7.

63. Ran, F.A., Hsu, P.D., Wright, J., Agarwala, V., Scott, D.A., and Zhang, F. (2013). Genome engineering using the CRISPR-Cas9 system. Nat. Protoc. *8*, 2281–2308. https://doi.org/10.1038/nprot.2013.143.

64. Lehtimäki, J.I., Rajakylä, E.K., Tojkander, S., and Lappalainen, P. (2021). Generation of stress fibers through myosin-driven reorganization of the actin cortex. eLife *10*, e60710. https://doi.org/10.7554/eLife.60710.

65. Kokate, S.B., Dixit, P., Poirah, I., Roy, A.D., Chakraborty, D., Rout, N., Singh, S.P., Ashktorab, H., Smoot, D.T., and Bhattacharyya, A. (2018). Testin and filamin-C downregulation by acetylated Siah2 increases invasiveness of Helicobacter pylori-infected gastric cancer cells. Int. J. Biochem. Cell Biol. *103*, 14–24. https://doi.org/10.1016/j.biocel.2018.07.012.

66. Pylvänäinen, J.W., Laine, R.F., Saraiva, B.M.S., Ghimire, S., Follain, G., Henriques, R., and Jacquemet, G. (2023). Fast4DReg - fast registration of 4D microscopy datasets. J. Cell Sci. *136*, jcs260728. https://doi.org/10.1242/jcs.260728.

67. Han, S.J., Oak, Y., Groisman, A., and Danuser, G. (2015). Traction microscopy to identify force modulation in subresolution adhesions. Nat. Methods *12*, 653–656. https://doi.org/10.1038/nmeth.3430.

Please cite this article in press as: Kokate et al., Calponin isoforms define the cell-type-specific organization and dynamics of actomyosin bundles, Current Biology (2025), https://doi.org/10.1016/j.cub.2025.10.081

STAR★METHODS

KEY RESOURCES TABLE

REAGENT or RESOURCE	SOURCE	IDENTIFIER
Antibodies		
Rabbit anti-Calponin-1	Abcam	Cat# ab46794 (EP798Y)
Rabbit anti-Calponin-2	Proteintech	Cat# 21073-1AP
Mouse anti-Calponin-3	Santacruz	Cat# SC271188
Mouse anti-Vinculin	Sigma-Aldrich	Cat# V9131
Rabbit anti-NM-IIA	BioLegend	Cat# 909801
Mouse anti-α-actinin-1	Sigma-Aldrich	Cat# A5044
Rabbit anti-GAPDH	Sigma-Aldrich	Cat# G9545
Bacterial and virus strains		
E. coli XL10 gold ultracompetent cells	This study	N/A
Chemicals, peptides, and recombinant proteins		
Alexa Fluor 488, 568 and 647 conjugated to phalloidin	Thermo Fisher Scientific	Cat# A12379, Cat# A1238, and Cat# A22287
Secondary antibodies conjugated to Alexa Fluor 488, 568 and 647	Thermo Fisher Scientific	Cat# A11001, Cat# A11004, Cat# A31571, Cat# A11034, and Cat# A21245
4’,6-diamidino-2-phenylindole, dihydrochloride (DAPI)	Thermo Fisher Scientific	Cat# D1306
HRP-conjugated goat anti–rabbit	Thermo Fisher Scientific	Cat# G21234
HRP-conjugated goat anti–mouse	Thermo Fisher Scientific	Cat# 31430
Cell Mask Deep red	Thermo Fisher Scientific	Cat # H32717
Epidermal growth factor	Peprotech	Cat# AF-100-15
Fibronectin	Merck	Cat# 1080938001
ProLong Glass Antifade mountant	Invitrogen	Cat# P36980
Vectashield Vibrance antifade mounting medium	Vector Laboratories	Cat# H-1700-10
Dimethyl sulfoxide (DMSO)	Sigma	Cat# D2650-5X10ML
Dulbecco’s modified Eagle’s medium (DMEM)	Euro Clone	Cat# ECB7501L
Fetal Bovine Serum (FBS)	GIBCO	Cat# 10500-064
10 U/ml penicillin, 10 mg/ml streptomycin, and 20 mM L-glutamine	GIBCO	Cat# 10378-016
FluoroBrite DMEM	GIBCO	Cat# A1896701
PLL-g-PEG	Surface technology	N/A
Silane	Sigma	Cat# GE17-1330-01
200 nm Yellow-Green fluorescent beads	Thermo Fisher Scientific	Cat# F8811
Acrylamide	Sigma	Cat# A4058
N,N’-methylenebisacrylamide	Sigma	Cat# M1533
Ammonium persulfate	Bio-Rad	Cat# 1610700
N,N,N’N’-tetramethylethylenediamine	Sigma	Cat# T9281
Sulfo-SANPAH	Sigma	Cat# 803332
N-(3-Dimethylaminopropyl)-N′-ethylcarbodiimide hydrochloride	Sigma	Cat# 03450
Critical commercial assays		
Mycoalert Mycoplasma Detection Kit	LONZA	Cat# LT07-418
FuGENE HD	Promega	Cat# E2312
jetPRIME (Polyplus transfection)	Biotop	Cat# 409-10
PureLink Genomic DNA Mini Kit	Thermo Fisher Scientific	Cat# K182001

(*Continued on next page*)

Please cite this article in press as: Kokate et al., Calponin isoforms define the cell-type-specific organization and dynamics of actomyosin bundles, Current Biology (2025), https://doi.org/10.1016/j.cub.2025.10.081

Continued

REAGENT or RESOURCE	SOURCE	IDENTIFIER
NucleoSpin Gel and PCR Clean-up	Macherey-Nagel, Vingmed	Cat# 740609.250
NucleoSpin Plasmid EasyPure	Macherey-Nagel, Vingmed	Cat# 740727.250
NEBuilder kit	New England BioLabs	Cat# E5520S
4%–20% gradient SDS-PAGE gels	Bio-Rad	Cat# 4561096
Trans-Blot Turbo transfer pack Mini Format	Bio-Rad	Cat# 170-4158
ECL pro substrate	Revvity	Cat# NEL122001EA
Experimental models: Cell lines		
Human osteosarcoma (U2OS) cells	This study	N/A
Hela cells	This study	N/A
NIH/3T3 cells	Leo Almeida-Souza (University of Helsinki, Finland)	N/A
U2OS EGFP-CAAX stable cells	This study	N/A
For Oligonucleotides used in this study see Tables S1, S2, and S3	N/A	N/A
Recombinant DNA		
CNN1 SMARTpool siRNA	Dharmacon	N/A
AllStars Neg. Control siRNA	Qiagen	Cat# 1027281
pSpCas9(BB)-2A-GFP-CNN2 guide1	This study	pPL1901
pSpCas9(BB)-2A-GFP-CNN2 guide2	This study	pPL1902
pSpCas9(BB)-2A-GFP-CNN2 guide3	This study	pPL1903
EGFP-CNN1	This study	pPL1370
mScarlet-CNN1	This study	pPL2006
EGFP-CNN3	This study	pPL1372
mScarlet-CNN3	This study	pPL2009
EGFP-CNN3ΔTail	This study	pPL2010
mScarlet-CNN3ΔTail	This study	pPL2011
GFP-β-actin	This study	pPL1281
GFP-Lifeact	This study	pPL1390
GFP-L-caldesmon	This study	pPL1374
GFP- α-actinin	This study	pPL0285
RFP- α-actinin	This study	pPL1423
EGFP-Tpm1.6	This study	pPL1126
EGFP-Tpm4.2	This study	pPL1128
GFP-NM-IIA	This study	pPL1436
GFP-NM-IIB	This study	pPL1437
Software and algorithms		
Fiji- ImageJ	N/A	N/A
Cell-IQ analyzer	CM Technologies	N/A
Cell Profiler	Molecular Devices	N/A
SlideBook 6.0	3I Intelligent Imaging Innovations	N/A
Ridge Detection	Fiji – ImageJ	N/A
MS Excel, PowerPoint, and Word	Microsoft	N/A
Geneious	Biomatters Limited	N/A
Origin	OriginLab Corporation	https://www.originlab.com/
MATLAB	Mathworks	https://se.mathworks.com/
R4.5.1	R Core Team	https://www.R-project.org/
Leica LAS X 3.7.5 16.7.2024	Leica Microsystems	N/A
Acquire SR 4.4 acquisition software/ SoftWoRx 7.0	GE Healthcare	N/A
Zen Black	Carl Zeiss Microscopy, LLC	N/A

Please cite this article in press as: Kokate et al., Calponin isoforms define the cell-type-specific organization and dynamics of actomyosin bundles, Current Biology (2025), https://doi.org/10.1016/j.cub.2025.10.081

EXPERIMENTAL MODEL AND SUBJECT DETAILS

Cell-lines and transfections

Human osteosarcoma (U2OS) cells (ATCC HTB-96, verified through STR profiling, and originally derived from a fifteen-year-old human female suffering from osteosarcoma), Hela cells, and NIH/3T3 cells were cultured in Dulbecco's modified Eagle's medium (DMEM) (ECB7501L, Euro Clone) containing high glucose (4.5 g/L), supplemented with 10 % FBS (10500-064, GIBCO), Pen-Strep-Glutamine solution (10378016, 100X, GIBCO) at 37°C, 5 % CO2 and 95 % relative humidity. The cell lines were routinely checked for mycoplasma contamination using the Mycoalert Mycoplasma Detection Kit (LT07-418, LONZA). Transfections were performed using FuGENE HD transfection reagent at 3.5:1 FuGENE HD/DNA ratio as per the manufacturer's protocol (E2312, Promega). Incubation time for transient transfections and for rescue experiments were 24 hours and 48 hours, respectively. Following transfection, cells were either fixed with 4 % paraformaldehyde or used for live-cell imaging experiments. The EGFP-CAAX cell-line was generated as previously described.[62]

METHOD DETAILS

Plasmids

Human *Cnn-1*, *Cnn-2*, *and Cnn-3* cDNAs were subcloned into pEGFP-C1 and pmScarlet-C1 vectors through Gibson assembly method. *Cnn-3 ΔC-tail* was constructed from *Cnn-3* full length plasmid (the primers used for cloning and are listed in Table S1). The assembled vectors were transformed into *E. coli* XL-10 ultracompetent cells. The constructs isolated from transformed bacteria were verified by Sanger sequencing by standard set of primers using Eurofins sequencing service (Eurofins Genomics, Germany). GFP-β-actin, GFP-Lifeact, GFP-L-caldesmon, RFP-/GFP-α-actinin-1, EGFP-Tpm1.6, EGFP-Tpm4.2, GFP-NMHC-IIA, and GFP-NMHC-IIB plasmids were available from previous studies. All the plasmids used in this study, along with their identification numbers, are listed in Table S2.

Generation of knockout cell-lines

Calponin-2 knockout cell lines were generated by CRISPR/Cas9 method as described previously.[18] Calponin-3 knockout cell line from a previous study[33] was used for generating Calponin-2&3 double knockout cell line. Three guide sequences targeting the exon 1 of human Calponin-2 gene (ENSG00000064666) were selected with specificity scores 93.04 %, 61.39 %, 57.31 % and efficiency scores 50.71 %, 68.22 %, and 55.83 % (Table S2). Oligonucleotides for cloning guide RNA into pSpCas9 (BB)-2A-GFP vector (48138; a gift from F. Zhang, Addgene, Cambridge, MA) were designed as described previously[63] (Table S3). The constructs were transfected to 18-24 hours U2OS cell cultures using Fugene HD transfection reagent. After 24 hours of transfection, cells were sorted with FACSAria II (BD), using low intensity GFP-positive pass gating, as single cells onto a 96-well plate supplemented with 10 mM HEPES and high FBS containing DMEM media. The knockout clones were confirmed at protein level by Western blotting using CNN2 and CNN3 -specific antibodies. Genomic DNA was isolated from the identified knockout clones and the amplified cDNA fragments from exon 1 were analyzed by Sanger sequencing (Eurofins genomics sequencing service) and next generation sequencing (NGS) at Genomics Laboratory (BIDGEN) (Institute of Biotechnology, University of Helsinki, Finland).

siRNA experiments

siRNA knockdowns were performed with jetPRIME transfection reagent (PolyPlus Transfection) according to manufacturer's instructions, using 5 nmol ON-TARGETplus human CNN1 SMARTpool siRNA (Dharmacon). CNN1 Target sequences were: 5′-UGGCA UCAUUCUUUGCGAA-3′, 5′-GGGUGAAGCCCCACGACAU-3′, 5′-CAGCAUGGCGAAGACGAAA-3′, 5′-GGCAUGGAGCACUGC GACA-3′. 20 nmol AllStars Neg. Control siRNA (1027281, Qiagen), was used as a negative control in all siRNA experiments. 48 hours incubation period was used to efficiently deplete the target protein.

Micropatterns

Glass coverslips (20 mm x 20 mm) (11961988, Thermo Fisher Scientific) were first washed with acetone for 10 min. After drying, clean coverslips were irradiated under a deep UV light using a mercury vapour lamp (Novascan Technologies, PSD-UV, λ = 185 and 254 nm) for 10 min. UV-treated cover slips were then incubated with 0.1 mg/mL solution of PLL-g-PEG (Surface technology, Switzerland) in 10 mM HEPES, pH-7.4 at room temperature for 30 min. The coverslips were then rinsed three times with MilliQ water and allowed to dry at room temperature before patterning with a micropattern mask. Cleaned cover slips were placed on each crossbow micropattern (1600 μm^2) designed on a custom-made 5'' quartz photomask (Compugraphics, United Kingdom) over a drop of MilliQ water (3-5 μL). The mask-covered substrates were UV-irradiated for 12 min, rinsed with MilliQ, dried and stored until further use. The micropattern coverslips were washed with 1X PBS three times before seeding cells on them.

Immunofluorescence stainings

The coverslips used for cell seeding were coated with 1 $\mu g/cm^2$ fibronectin (10 μg/ml, 11080938001, Merck) for 1 hour at room temperature. The coverslips were washed three times with 1X PBS solution before seeding cells on them. After cell attachment and spreading (6 hours), they were fixed in 4 % paraformaldehyde in PBS for 10 min at room temperature. Following fixation, the cells

Please cite this article in press as: Kokate et al., Calponin isoforms define the cell-type-specific organization and dynamics of actomyosin bundles, Current Biology (2025), https://doi.org/10.1016/j.cub.2025.10.081

were permeabilized with 0.1 % Triton X-100 in PBS. Fixed cells were incubated in blocking solution (5 % BSA in PBS) for 1 hour at room temperature followed by staining using various primary antibodies at proper dilutions using manufacturer's instructions. The cells were washed three times with 0.02 % Tween 20 containing PBS (PBST) and were incubated with secondary antibodies for 1 hour at room temperature in dark. The cells were simultaneously counter stained with DAPI. The coverslips were washed three times with PBST and mounted in ProLong Glass Antifade mountant (P36980, Invitrogen).

Fluorescence-recovery-after-photobleaching (FRAP)

FRAP experiments were performed at 37 °C, 5 % CO2, and 95 % relative humidity using 3I Marianas imaging system (3I Intelligent Imaging Innovations)-Yokogawa CSU-X1 M1 5000 rpm spinning disk confocal microscope using ×63/1.2 W C-Apochromat Corr WD = 0.28 M27 water immersion objective. Image acquisition was performed using Andor Neo sCMOS camera and FRAP analysis was performed using Fiji ImageJ 1.54f software (please see; section 17(v) for image analysis). The following parameters were used for GFP-β-actin, EGFP-Tpms, and GFP-α-actinin-1 FRAP assays: pre-bleach (laser: 488 nm, 150 mW power with 70 % laser intensity, 1 frame per 5 s, 4 frames), bleach (laser: 488 nm, 150 mW power with 100% laser intensity, 1 frame per 4 ms, 4 frames), post-bleach acquisition (laser: 488 nm, 150 mW power with 70 % laser intensity, 1 frame per 5 s, 150 frames). For GFP-L-caldesmon and EGFP-CNN1/CNN3/CNN3ΔTail FRAP assays: pre-bleach (laser: 488 nm, 150 mW power with 70 % laser intensity, 1 frame per 200 ms, 4 frames), bleach (laser: 488 nm, 150 mW power with 100 % laser intensity, 1 frame per 4 ms, 4 frames), post-bleach acquisition (laser: 488 nm, 150 mW power with 70 % laser intensity, 1 frame per 200 ms, 50 frames followed by 1 frame per 10 sec, 300 frames).

FRAP experiments for GFP-Myosin IIA and IIB were performed on a Zeiss Cell Discoverer 7 microscope equipped with a confocal LSM900. After finding a suitable cell, a single high-resolution image (805×805 pixels) was acquired to identify the ventral stress fibers with 488 nm laser excitation. Then, a suitable spot of 161×161 pixels was zoomed in to acquire time-lapse images for fast scanning without signal averaging. All scannings were done in Nyquist criteria. After acquiring 5 pre-bleach images at 1 fps, photobleaching was performed on ventral stress fibers within a 4×12 μm rectangular ROI, rotated to ensure uniform photobleaching on a 4 μm length of individual stress fibers, and then imaging was continued until 10 mins at the same frame rate. Image processing was later performed on Fiji ImageJ, where the movement of the cell was rectified manually and mean intensity within a rectangular ROI, drawn strictly on the photobleached ventral stress fiber, was plotted against time post bleaching. Local intensity change was normalized with intensity from a reference ROI on the same stress fiber in an unbleached region and the cell-free background intensity was subtracted from each value. The data were then fitted to the Exponential Association 1 function in Origin Pro 2024b to extract the recovery time.

Traction force microscopy

Hydrogel preparation

1 ml bind silane solution (7.14 % Plus One Bind silane (GE17-1330-01, Sigma) and 7.14 % acetic acid in absolute EtOH) was added to 35 mm glass bottom dishes (D35-14-1, CellVis) and incubated for 30 min at room temperature. Wells were then washed twice with 2 ml of EtOH and allowed to air-dry. For the hydrogels (~10 kPa), 1.7 μl fluorescent beads (FluoSpheresTM Carboxylate-Modified Microspheres, 200 nm Yellow-Green, F8811) were sonicated and added to 500 μl hydrogel mix (94 μl 40 % acrylamide (A4058, Sigma) and 50 μl N,N'-methylenebisacrylamide (M1533, Sigma) in PBS). 5 μl 10 % ammonium persulfate (1610700, Bio-Rad) and 1 μl N,N,N'N'-tetramethylethylenediamine (T9281, Sigma) was added to the hydrogel mixture to induce polymerisation and the mixture vortexed. 11.8 μl of this mixture was added to the dishes, and clean 13 mm glass coverslips were placed on top. Following 1 hour incubation at room temperature, PBS was added to the dishes and the glass coverslips removed from the hydrogel. The surface of the hydrogels was activated by incubating the gels for 30 minutes at room temperature in 500 μl 0.2 mg/ml Sulfo-SANPAH (803332, Sigma) and 2 mg/ml N-(3-Dimethylaminopropyl)-N′-ethylcarbodiimide hydrochloride (03450, Sigma) in 50 mM HEPES, before irradiation with UV light for 10 min. Gels were washed four times with PBS and coated with 10 μg/ml fibronectin overnight at 4°C.

Cell seeding and imaging

Wild-type, CNN2&3 knockout and CNN-2&3 knockout-siCNN1 cells were seeded onto fibronectin-coated ~10 kPa gels for 2 hours at 37°C prior to staining them with CellMask Deep red to visualize the cell edge. The old media containing CellMask Deep red was replaced with DMEM media containing 10 mM HEPES. Images of stained cells and fluorescent nano beads beneath the cells were acquired in z-stacks at 37 °C, 5 % CO_2, and 95 % relative humidity using 3I Marianas imaging system (3I Intelligent Imaging Innovations) under blue (solid state 488 nm/150 mW) and red (solid state 640 nm/100 mW) lasers before trypsinization. The x/y/z positions of cells were recorded, and were applied to revisit the positions post-trypsinization to capture the image of nanobeads and confirm cell detachment post-trypsinization (microscope specifications and imaging setup as described before in live-cell imaging section).

Fixed-cell imaging

Immunofluorescence samples were imaged using Leica DM6000B fully motorized upright fluorescence microscope equipped with a 63x/1.40-0.60 HCX PL APO Lbd.bl. Oil wd=0.10 objective and following optical filters: DAPI-5060C (ex 377/50, em 447/60), CFP-2432C (ex 438/24, em 483/32), GFP-4050B (ex 466/40, em 525/50), TRITC-B (ex 543/22, em 593/40), LED-mCherry-A (ex 578/21, em 641/75), Cy5-4040C (ex 628/40, em 692/40) (IDEX Health & Science, LLC, USA). The images were acquired using Hamamatsu Orca-Flash4.0 V2 sCMOS camera with 2048 × 2048 pixels image resolution. The images were processed using LAS X 3.7.5 16.7.2024 and Fiji imageJ (version-1.54f) softwares.

Please cite this article in press as: Kokate et al., Calponin isoforms define the cell-type-specific organization and dynamics of actomyosin bundles, Current Biology (2025), https://doi.org/10.1016/j.cub.2025.10.081

Live-cell imaging

Wild-type and knockout cells were plated on fibronectin-coated 35 mm glass bottom dishes (81158, Ibidi) for 2 hours at 37°C, 5 % CO2, and 95 % relative humidity. For rescue experiments, the CNN2&3 knockout cells were transfected with EGFP-CNN1, CNN3 and CNN3ΔTail plasmids for 48 hours. Old media was replaced with Fluorobrite DMEM (Gibco, A1896701), containing 10 % FBS, glutamax and 25 mM HEPES before starting the imaging.

Wide-field imaging

The retrograde flow of transverse arcs in wild-type and knockout cells was imaged using GE Deltavision ultra microscope (customized Olympus IX-73 inverted microscope) equipped with a 100x 1.4 NA 0.13 WD oil objective and single band pass excitation/emission filters. The images were captured for 10 mins with 5 sec interval using Pco edge 4.2ge sCMOS camera at 2040 x 2040 pixels image resolution. Automated acquisition was performed with Acquire Ultra software. Automatic post-acquisition processing and deconvolution was performed simultaneously during the time-lapse imaging using in-built task builder deconvolution and correction platform. Ratio (conservative) method with 10 iterations and 50 camera intensity offset was utilized for deconvolution.

3D-SIM super-resolution imaging

Imaging was performed as described previously.[18,64] Briefly, all 3D-SIM images were captured in z-increment of 0.125 mm at room temperature using GE Deltavision OMX super resolution upright microscope (GE Healthcare) with a Plan-Apo N ×60/1.42 Oil immersion objective, equipped with 405-, 488-, 568-, 640 nm diode laser lines and three sCMOS detector cameras, operated through Acquire SR 4.4 acquisition software. Reconstruction and alignment of different channels was performed using SoftWoRx 7.0 with the point spread function available from the manufacturer. Immersion oil was used as per the calculation for samples with two or more fluorophores using GE immersion oil calculator. Imaging arrays of 1024 x 1024 or 512 x 512 were used, both with pixel size of 0.08 mm and 0.125 mm (x/y and z).

The Zeiss Elyra Lattice SIM (Structured Illumination Microscopy) and Zeiss LSM900 Airyscan2 were used to image fixed cells expressing GFP-α-actinin-1, GFP-NM-IIA, GFP-NM-IIB, GFP-Tpm1.6, and GFP-Tpm4.2 in conjunction with Alexa Fluor 568 Phalloidin or Alexa Fluor 647 Phalloidin. Cells were seeded on fibronectin coated 35 mm glass bottom Ibidi dishes for overnight before fixation with warm 4% PFA. Post fixation, the cells were washed with 1×PBS thrice, permeabilized with 0.1% Triton X-100 in 1×PBS for exactly 10 mins, then incubated in a blocking solution of 2.5% BSA in 1×PBS. Finally, the blocking solution was replaced with fluorescent phalloidin solution (1:100 dilution in 2.5% BSA in 1× PBS) for at least 10 hours at 4°C only to be replaced with 1×PBS immediately prior to imaging. For Lattice SIM, the structured illumination generated by a 32 μm grating was used to image 13 phases for each slice in the Z-stack images acquired with a 63× oil immersion objective. The 'green' and 'red/far-red' fluorescence emissions were split into two pre-aligned Hamamatsu C15440-20UP CMOS cameras using a dichroic beam splitter. SIM reconstruction was performed with in-built image processing algorithms of the Zen Black software depending on the signal strength (Wiener filter strength of 'Good SNR' or 'Low SNR').

A Zeiss Cell Discoverer 7 microscope equipped with LSM900 Airyscan2 module was used to image fixed U2OS cells co-expressing GFP-NM-IIA and TagRFP-α-actinin-1 in conjunction with Alexa 647 Phalloidin. A 50× water immersion objective was used to acquire Z stacks in 3 wavelength channels, and Airyscan post processing was done on the Zen Black software with a sharpness filter strength of 'Standard' or 'Low' depending on the signal-to-noise-ratio of images.

Laser ablation

Wild-type and CNN2&3 double knockout U2OS cells expressing pEGFP-C1-LifeAct, and wild-type USOS cells expressing pEGFP-C1-LifeAct and pmScarlet-CNN1 were seeded on CYTOOchip fibronectin-coated crossbow micropattern coverslips (19.5×19.5 mm) placed in a 35 mm culturing dish for overnight. Prior to live-cell imaging, the cell-seeded coverslip was mounted into a CYTOOchamber 35 mm imaging chamber and cells were incubated in Fluorobrite DMEM media (#A18967-01 500 ml, GIBCO) supplemented with 10% FBS, 1× PSG, and 10 mM HEPES (pH-7.4). The ablation experiments were carried out on a modified Olympus FV3000 inverted confocal laser scanning microscope (qCSI Multimodal microscope, Raman microscopy facility, University of Helsinki, Finland) at 37°C, 5% CO2 at 95% relative humidity. Imaging was performed at 1 fps for 1 min duration with a 60× water immersion objective by one-way scanning with Galvano-mirrors. EGFP-C1-LifeAct was excited with a 488 nm laser and fluorescence was detected with the HSD1 PMT (500-551) (512×512-pixel image size). After acquiring 3 pre-ablation images, photoablation was performed by illuminating a point-ROI placed midway on a ventral stress fiber of uniform thickness for 50 ms using a 3 W, 80 MHz femtosecond pulsed laser tuned at 900 nm wavelength, with 70% laser power (~166 mW at objective).

Data preprocessing, time-lapse image analysis for stress fiber retraction measurements were carried out using Fiji ImageJ, where the lengths of the ablated stress fibers were measured in each frame. Kindly note that only the 'bottom-half' of the ablated stress fibers from the ablation point was measured for consistency. The length difference between each frame, i.e., the retraction distance L(t), was plotted against time elapsed post-ablation and fitted to the Kelvin-Voigt equation for viscoelastic materials: $L(t)=L_0\,(1\text{-e }\hat{}(\text{-}t/\tau)\,)+D_a$, where L_0 is the maximum retraction distance, τ is the retraction time constant, and D_a is the length of the material destroyed during ablation. Data fitting and parameter extraction were performed using Origin Pro 2024b.

Please cite this article in press as: Kokate et al., Calponin isoforms define the cell-type-specific organization and dynamics of actomyosin bundles, Current Biology (2025), https://doi.org/10.1016/j.cub.2025.10.081

Wound healing assay

Collective migration of wild-type and CNN2 knockout U2OS cells was studied by wound healing assay as reported previously.[65] Briefly, the 5 × 10^5 cells were plated in a 12-well culture plate and incubated for 18-24 hours to form uniform monolayer of cells. A scratch was made at the mid area of every well using a 200 μl micropipette tip, the media containing the floating cells was replaced with 10% FBS + 10 mM HEPES containing-DMEM media, and time-lapse imaging was performed using Cell-IQ imaging system by Nikon Plan Fluor 10x/0.30 Ph1 DL objective (phase-contrast mode) and Q imaging Retiga EXi camera (pixel no. (W× H): 1392 × 1040, 0.7 μm = 1 pixel). The images were captured and processed with 2 x 2 binning and 10 min intervals for 24 hours with Cell-IQ Imagen 4.1.0 software. The captured images were stitched together using Cell-IQ Analyser 4.4.0 software and analyzed to obtain the wound area (% and μm^2) and the length of the wound created at time 0 and covered after 24 h of imaging. The values obtained were applied to plot a line graph as mean of percent area covered by wild-type, Calponin-2 KO, Calponin-3 KO and CNN2&3 KO U2OS cells.

Random cell migration assay

Random cell migration assay was monitored as reported previously.[62] The cells were plated in fibronectin-coated 12-well plates before imaging. For rescue experiments, CNN2&3 knockout cells were transfected for 48 hours before starting the imaging. Phase contrast (and fluorescent imaging for rescue experiments) time-lapse imaging was performed using Cell-IQ imaging system as described in the 'wound healing assay' section above. In rescue experiments, transfected cells expressing moderate levels of EGFP- or mScarlet-tagged calponins were selected for analysis. Colliding and dividing cells were omitted from the analysis.

High-content imaging

The shapes and sizes of cells were analyzed using ImageXpress Nano Automated Imaging System (Molecular Devices) with ×20/0.45S Plan Fluor ELWD, WD8.2–6.9mm water immersion objective, and 409, 495, 593, and 660 nm dichroic filters. The images were processed in Cell-Profiler 3.1.8 automated image analysis software. Post-imaging, thresholding and segmentation settings were implemented as reported previously.[18] For rescue experiments, EGFP-tagged CNN1, CNN3 and CNN3ΔTail plasmids were used.

In-vitro transwell invasion assay

The transwell invasion assay was performed using 6.5 mm with 8.0 μm pore polycarbonate membrane transwell inserts (CLS3422-48EA, Sigma-Aldrich) as per manufacturer's guidelines. For invasion assay, 5 × 10^4 cells were seeded into the upper chamber suspended in low serum containing media, whereas the bottom chamber contained high serum containing media supplemented with 25 ng/ml epidermal growth factor (AF-100-15, Peprotech) as a chemoattractant. The transwell chamber was coated with 300 μg/ml matrigel. After 6 hours incubation at 37 °C, the inserts were fixed and the inner surfaces of the inserts were scrapped with wet cotton plug followed by gentle washing with phosphate buffer saline, pH-7.4. The inserts were further permeabilized (0.1 % Triton X-100), and counterstained with DAPI and phalloidin 488 dyes. The inserts were mounted on slides with Vectashield Vibrance antifade mounting medium (H-1700-10, Vector Laboratories), and imaged using the fixed-cell imaging protocol.

Western blotting

1.2 x 10^6 cells were seeded on 6-well plates 18-24 hours before harvesting. Cells were washed twice with ice-cold PBS solution and harvested with a cell scraper into lysis buffer (50 mM Tris-HCl pH-7.5, 150 mM NaCl, 1 mM EDTA, 10 % Glycerol, 1 % Triton X-100) supplemented with protease inhibitors cocktail. All preparations were conducted on ice. Protein concentrations were determined with DC Protein assay (5000111, Bio-Rad) and equal amounts of the total cell lysates were mixed with Laemmli Sample Buffer, boiled, and run on 4–20 % gradient SDS-PAGE gels (4561096, Bio-Rad). Proteins were transferred to 0.2 μm nitrocellulose membrane (1704158, Trans-blot turbo transfer pack, Biorad) using Trans-Blot Turbo transfer system (1704150, Biorad). The membranes were blocked for 1 hour at room temperature either with 5 % BSA or skimmed milk in PBS-T (0.05 % Tween-20) followed by overnight shaking incubation with primary at 4 °C. Next day, the membranes were washed three times in 0.1 % TBS-T and incubated with respective HRP-conjugated secondary antibodies for 1 hour at room temperature. Proteins were visualized using western lightning ECL pro substrate (NEL122001EA, Revvity) in the ChemiDoc XRS+ System (1708265, Biorad) and the protein bands were quantified using Image Lab™ (1709690, Biorad) and Fiji ImageJ 1.54f software. GAPDH was used as a loading control.

Image analysis

Stress fiber thickness analysis

Cells were plated on fibronectin-coated coverslips for 14 h before fixation and stained with Alexa Fluor 488 Phalloidin (1:400; A12379). The images were acquired by using a wide-field microscope. The thickness of stress fibers in U2OS cells were quantified with Ridge detection plugin from Fiji ImageJ. The parameters used were: line width 20.0, high contrast 230, low contrast 100, sigma 6.57, low threshold 0.0, and upper threshold 0.34. Blind analysis was performed for the phenotypic quantification of thickness and alignment of stress fibers. For stress fiber thickness, the stress fibers were categorized into three groups based on their width: 1. 'Thick', 2. 'Moderate', 3. 'Thin'.

Stress fiber alignment analysis

For stress fiber alignment, the stress fibers were categorized into three groups based on their organization: 1. 'Aligned', 2. 'Intermediate', 3. 'Disorganized'. The 'intermediate' organization was defined as where the stress fibers showed a mix between organized and bent organization, that was in between normal 'aligned' and abnormal 'disorganized' organization. For binary segmentation, Ridge detection plugin from Fiji ImageJ was used. The parameters used were: line width 20.0, high contrast 230, low contrast 100, sigma 6.57, low threshold 0.0, and upper threshold 0.34.

Focal adhesion segmentation/ size analysis

Immunofluorescence images stained for focal adhesion (FA) marker proteins vinculin were analyzed for the number of FAs in each parent cell, their individual areas, aspect ratios, and the minimum distance of the FAs from the cell edge using a home-built Fiji (ImageJ) macro. Briefly, the main image was duplicated, then one copy was smoothed by a Median filter of radius 1 pixel (using *Process>Filters>Median*), and the other copy was convolved (*Process>Filter>Convolve*) with an edge filter kernel where the pixel size of the kernel matrix was approximately twice the width of general FA structures. The smoothed image was then divided with the convolved image to remove large bright structures (like non-specific staining in the nucleus). This resultant image was further despeckled (*Process>Noise>Despeckled*) and FFT bandpass filters (*Process>FFT>Bandpass Filter*) were applied to remove general pixel noise. An appropriate gamma correction (*Process>Math>Gamma*) was applied on the filtered image to highlight the FAs against background, after which intensity thresholding was performed using the Otsu method that resulted in the maximal selection of FA structures. The macro enables live tuning of various parameters until the user can determine the most robust FA segmentation for the target image. Finally, using the *Analyze Particles* function, the FA structures were extracted based on a size range and only the structures present within user-defined cell boundaries were used for analysis. Cells that were in contact with neighboring cells were discarded from the analysis.

Analysis of focal adhesion distribution

For quantifying the spatial distribution of FAs, the FA percentage was analyzed in two regions of the cells. Cell edge was defined by distance of 5 μm taken from cell periphery and rest of the region as cell center/rear. The distance from the cell edge was calculated by finding the closest pixel coordinate to the respective FA ROI centroids. The percentage of adhesions in these regions was correlated to the total number of adhesions in the same cell.

FRAP analysis

FRAP data in all figures were analyzed as previously reported.[18,62,64] Briefly, to measure the photo-recovery of the bleached area, a neighboring area along the same stress fiber was identified and the fluorescence intensity of the beached area was divided by the fluorescence intensity of the non-bleached or control area. The background fluorescence intensity was subtracted from the fluorescence intensities of the bleached and the control area. Microsoft (MS) Excel was used to calculate the mean recovery (%) and recovery half-time (s) across replicates in different groups.

TFM analysis

Bead images taken before and after cell removal were aligned using the Fast4Dreg plugin in Fiji,[66] and bead tracking and force measurements were performed using TFM software[67] in MATLAB (Mathworks, version 2020a). Displacement field calculation was performed using high-resolution subsampling of beads, subpixel correlation via image interpolation, no outward deformation expected selected, with a template size of 21 pixels and maximum displacement of 20 pixels. Vector outliers were filtered and a normalized displacement residual threshold of 2 was used for displacement field correction. Finally, for force field calculation, Fourier transform traction cytometry (FTTC) was used with a regularization parameter on 0.0001. Cell masks were generated from CellMask deep red images and overlaid onto the traction maps using R (A Language and Environment for Statistical Computing. R Foundation for Statistical Computing, Vienna, Austria. https://www.R-project.org/) to obtain mean traction per cell.

Analysis of stress fiber breakage events

Following live-cell imaging of EGFP-tagged β-actin in wild-type and knockout cells for 30 mins using GE Deltavision ultra microscope, the breakage events of ventral stress fibers were analyzed minutely using Fiji imageJ. The stress fiber area showing the breakage event and time point of the breakage event occurrence was recorded using Fiji imageJ ROI tool. The extent of stress fiber retraction and the number of breakage events observed in 30 mins time frame for a given sample was recorded was used to plot the scatter plot using MS excel.

Transverse arc kymograph analysis

Transverse arcs retrograde flow kymograph analysis was conducted using Fiji ImageJ kymograph drawing tool. Live-cell imaging of EGFP-tagged β-actin expressing cells was carried out for 10 mins using GE Deltavision ultra microscope. Leading edge of cell showing uniform flow of transverse arcs was selected and a line was drawn from cell periphery to cell center denoting the direction of arcs flow. Next, kymograph analysis tool (*plugins>kymograph>kymograph builder*) was used for the selected cell area. Lines were drawn from at least 2-3 other areas in the same cell to maintain consistency in retrograde flow rate analysis. Distances of the transverse arc movement were measured from the obtained kymographs by drawing a vertical line representing the arc flow from cell periphery to cell center. The rate of transverse arc flow (μm/min) was obtained by dividing the distance of transverse arc flow (μm) by the length of the time-lapse imaging (10 mins). The values obtained were used to plot a scatter plot for the given group using MS excel.

3D-SIM line scan analysis

3D-SIM images were constructed from average intensity projections of Z-stacks using Stacks/Z-project and analyzed using 3D imageJ plugins in Fiji ImageJ 1.53c software. For line scan analysis of α-actinin-1/ NM-IIA/ NM-IIB, Tpm1.6/ Tpm4.2 in wild-type and knockout cells, stress fibers showing clear periodic pattern of EGFP-α-actinin-1 were chosen for line scan analysis. 2.5 μm line scan ROIs were drawn randomly along the stress fibers and the corresponding intensities for the green channel indicating EGFP-α-actinin-1/ NM-IIA/ NM-IIB, Tpm1.6/ Tpm4.2 expression were recorded. The individual line scans were normalized from 0 to 1 scale by dividing each fluorescence intensity at a given point with the highest fluorescence intensity recorded in that line scan. The final graph

Please cite this article in press as: Kokate et al., Calponin isoforms define the cell-type-specific organization and dynamics of actomyosin bundles, Current Biology (2025), https://doi.org/10.1016/j.cub.2025.10.081

represents the mean of all normalized line scans for respective cell line and indicates the number of α-actinin-1/ NM-IIA/ NM-IIB, Tpm1.6/ Tpm4.2 foci recorded in a 2.5 μm line scan along stress fibers.

QUANTIFICATION AND STATISTICAL ANALYSIS

Blind analysis was performed to quantify stress fiber thickness and alignment by randomly mixing phalloidin-stained images from all groups into a single pool. The images were then categorized into three groups based on stress fiber thickness: ‘thick,’ ‘moderate,’ and ‘thin’ and three groups based on fiber alignment: ‘aligned,’ ‘intermediate,’ and ‘disorganized.’ After assessing stress fiber thickness and alignment, the images were reassigned to their original groups, and bar diagrams were created in MS Excel, showing the number of cells in each group exhibiting the three phenotypes. Groups were compared with Kruskal-Wallis ANOVA followed by Dunn’s multiple comparison test. The half-time recovery measurement in FRAP experiments were performed manually by calculating the time required for a protein to recover to half of its pre-bleach fluorescence intensity following photobleaching. Statistical analysis and graph construction for intensity line profiles in all experiments were conducted using MS Excel and OriginPro 2024b (10.1.5.132-academic, OriginLab Corporation). Statistical tests were performed for paired/ unpaired samples using one-tailed Student’s t-tests with Welch’s correction and for more than two sample groups using one way ANOVA, followed by Tukey’s post-hoc analysis in OriginPro 2024b.